JGR Atmospheres

RESEARCH ARTICLE
10.1029/2022JD037544

Key Points:

- Methane warming peaks at a pCH_4:pCO_2 ratio of 0.1, with global-mean surface warming <7 K
- Uneven meridional methane radiative forcing and changes to atmospheric circulation determine the equator-to-pole temperature difference
- 3D modeling is important to fully capture methane's cooling effect for pCH_4:pCO_2 ratios greater than 0.1

Correspondence to:
J. K. Eager-Nash,
J.K.Eager@exeter.ac.uk

Citation:
Eager-Nash, J. K., Mayne, N. J., Nicholson, A. E., Prins, J. E., Young, O. C. F., Daines, S. J., et al. (2023). 3D climate simulations of the Archean find that methane has a strong cooling effect at high concentrations. *Journal of Geophysical Research: Atmospheres*, *128*, e2022JD037544. https://doi.org/10.1029/2022JD037544

Received 22 JUL 2022
Accepted 19 FEB 2023

3D Climate Simulations of the Archean Find That Methane has a Strong Cooling Effect at High Concentrations

J. K. Eager-Nash[1], N. J. Mayne[1], A. E. Nicholson[1], J. E. Prins[1,2], O. C. F. Young[1], S. J. Daines[3], D. E. Sergeev[1,4], F. H. Lambert[4], J. Manners[1,5], I. A. Boutle[1,5], E. T. Wolf[6,7,8], I. E. E. Kamp[2], K. Kohary[1], and T. M. Lenton[3]

[1]Department of Physics and Astronomy, University of Exeter, Exeter, UK, [2]Kapteyn Astronomical Institute, University of Groningen, Groningen, The Netherlands, [3]Global Systems Institute, University of Exeter, Exeter, UK, [4]Department of Mathematics and Statistics, University of Exeter, Exeter, UK, [5]Met Office, Exeter, UK, [6]Laboratory for Atmospheric and Space Physics, University of Colorado Boulder, Boulder, CO, USA, [7]NASA NExSS Virtual Planetary Laboratory, Seattle, WA, USA, [8]NASA GSFC Sellers Exoplanet Environments Collaboration, Greenbelt, MD, USA

Abstract Methane is thought to have been an important greenhouse gas during the Archean, although its potential warming has been found to be limited at high concentrations due to its high shortwave absorption. We use the Met Office Unified Model, a general circulation model, to further explore the climatic effect of different Archean methane concentrations. Surface warming peaks at a pressure ratio pCH_4:pCO_2 of approximately 0.1, reaching a maximum of up to 7 K before significant cooling above this ratio. Equator-to-pole temperature differences also tend to increase up to $pCH_4 \leq 300$ Pa, which is driven by a difference in radiative forcing at the equator and poles by methane and a reduction in the latitudinal extend of the Hadley circulation. 3D models are important to fully capture the cooling effect of methane, due to these impacts of the circulation.

Plain Language Summary The Archean is a period in Earth history spanning approximately 4 to 2.5 billion years ago. During this period oxygen concentrations were much lower than today, which in turn allowed methane concentrations to be much higher during the Archean. Methane would have been produced by microbes, and depending on the exact nature of the ecosystem could have led to a wide range of atmospheric concentrations. Using a three-dimensional climate model and with various methane concentrations in the atmosphere we show that the warming effect of methane first increases and then, at high concentrations, decreases. This decrease is stronger than those found in previous studies using one-dimensional (single column) atmosphere models. We find that methane can only warm the Archean by up to 7 K.

1. Introduction

Methane (CH_4) is thought to have played an important role as a greenhouse gas in warming the Archean Earth (Catling & Zahnle, 2020; Haqq-Misra et al., 2008). The Archean is the geological eon spanning 4.0–2.5 billion years ago (Ga). The Archean was believed to be oxygen poor, with oxygen concentrations less than 3×10^{-6} of the present atmospheric level (PAL) (B. S. Gregory et al., 2021), which allowed reduced gases, such as methane, to accumulate in the atmosphere (Catling et al., 2001). Here, we look to understand the potential role of methane, and to a lesser extent carbon dioxide (CO_2), on the Archean climate using a three-dimensional general circulation model (GCM), at various carbon dioxide concentrations. The use of a GCM further allows an understanding to be gained of the effect of methane on the global mean climate and the meridional temperature structure.

The Archean could have supported high methane concentrations at various points in its history (e.g., Figure 5 in Catling & Zahnle, 2020). A primitive pre-photosynthetic biosphere would effectively turn reductant (electron donors) from mantle inputs or oxidation of the crust into reduced organic carbon and ultimately methane (e.g., Nicholson et al., 2022). As methane will be photolyzed to hydrogen at high altitude, atmospheric methane levels are then determined by the balance between surface net reductant (hence methane) input, and hydrogen escape (Claire et al., 2006; Goldblatt et al., 2006; Kharecha et al., 2005). Kharecha et al. (2005) used a coupled ecosystem-atmosphere model to suggest that the early Archean biosphere could have sustained methane concentrations between 100 and 35,000 ppm (equivalent to 10–3,500 Pa in surface partial pressure for a 10^5 Pa atmosphere). Subsequent evolution of increasingly productive photosynthetic biospheres and ultimately oxygenic photosynthesis could increase methane concentrations as they increase the net reductant input via oxidation of crustal material (primarily Fe, Walker, 1987). This is supported by a depletion in organic carbon-13 in deep water sediments at 2.7 Ga (Eigenbrode & Freeman, 2006). After the great oxidation event, the concentration of methane as a minority gas in an oxic atmosphere will be controlled by the balance between primarily biological production and photochemistry, where the net biological flux to the atmosphere will be controlled by ecosystem structure and biogeochemical cycling hence methane oxidation within the surface environment (Daines & Lenton, 2016).

Updates to the high-resolution transmission molecular absorption database (HITRAN) have led to work finding that earlier studies have overestimated methane's potential to warm the Archean (Byrne & Goldblatt, 2015). Previously, Haqq-Misra et al. (2008) found that methane, ethane and the subsequent formation of longer chain hydrocarbons can provide significant warming. However, updates to HITRAN (L. Brown et al., 2013; Rothman et al., 2013) show an increase in the shortwave absorption by methane that was previously underestimated, leading to a decrease in tropopause radiative forcing by methane at high concentrations (see discussion in Byrne & Goldblatt, 2014). This was found to lead to the greenhouse effect of CH_4 becoming offset by strong shortwave absorption by methane in the atmosphere (Byrne & Goldblatt, 2015). Using a 1D radiative convective model (RCM) Byrne and Goldblatt (2015) found that surface warming due to methane is diminished at 100 Pa (0.1% by volume), with shortwave cooling dominating longwave heating above this. Methane shortwave radiative forcing has also been investigated for the modern Earth (Byrom & Shine, 2022; Collins et al., 2018; Etminan et al., 2016). Byrom and Shine (2022) found that methane's warming of the stratosphere by absorption of shortwave radiation can enhance methane longwave radiative forcing.

During the Archean, the Sun's luminosity was 75%–80% of the present day value (Gough, 1981). As discussed in Charnay et al. (2020), as the Sun fuses hydrogen into helium the mean molecular weight of the Sun's core increases. The core then contracts and warms to maintain the balance between the pressure gradient and gravitational forces. This increases the rate of fusion, which causes the solar flux to increase with time. Under present atmospheric conditions the Earth is predicted to have been globally ice covered (known as a snowball state) prior to ~2.0 Ga (Kasting & Catling, 2003). However, there is ample evidence that the Earth was not in a snowball state (e.g., see Feulner, 2012; Charnay et al., 2020). This was termed the faint young Sun (FYS) paradox (Sagan & Mullen, 1972), with uncertainty over what kept the early Earth warm. The resolution of the FYS paradox is likely to be due to increased greenhouse gas concentrations during the Archean, particularly carbon dioxide (Charnay et al., 2020) as well as methane.

Geological evidence has been used to predict CO_2 concentrations through the Archean. Mass balance calculations from CO_2 dissolved in rainwater give estimates of CO_2 10–50 PAL (340–1,700 Pa) at 2.7 Ga (Driese et al., 2011; Sheldon, 2006), although this may be a lower limit (Catling & Zahnle, 2020). Another method using chemical compositions of paleosols predicts CO_2 85–510 PAL (3,000–15,000 Pa) at 2.77 Ga and 78–2,500 PAL (2,000–75,000 bar) at 2.75 Ga (Kanzaki & Murakami, 2015). A more recent approach using oxidation of fossilized micrometeorites from 2.7 Ga (Tomkins et al., 2016) suggests a lower limit for atmospheric CO_2 of 32% (32,000 Pa) (Huang et al., 2021), although debate remains over these estimates, with a lower surface pressure offering an alternative solution to explain the micrometeorite oxidation (Rimmer et al., 2019).

General Circulation Models (GCMs), which are three-dimensional models attempting to capture the main processes determining the planetary climate, have played an important role in understanding the climate of the Archean (Charnay et al., 2013, 2020; Kunze et al., 2014; Le Hir et al., 2014; Wolf & Toon, 2013). GCMs have been used to show that compared to 1D models, lower amounts of CO_2 are required to maintain global surface temperatures of 15°C, and more importantly, avoid a full glaciation (Charnay et al., 2013; Wolf & Toon, 2013). Furthermore, the use of GCMs has found that potential reductions in land fraction and albedo during the Archean, as well as a reduction in cloud condensation nuclei may have helped to keep the early Earth warm (Goldblatt et al., 2021; Wolf & Toon, 2014). GCMs have also been used to explore the potential for glaciations at the end of the Archean (Teitler et al., 2014), alongside being combined with models of carbon cycling to investigate the plausibility of hot Archean climates (Charnay et al., 2017).

In this work we extend the 1D work of Byrne and Goldblatt (2015) by exploring the 3D effects of changing the methane concentration using the Met Office Unified Model (UM) GCM. First we outline the model configurations used for our Archean-like Earth simulations using the UM in Section 2. The results are presented in Section 3 where we demonstrate that methane has a maximum potential global warming of up to 7 K. We then go on to show that methane changes the equator-to-pole temperature differences by changing the meridional circulation and the radiative forcing at the poles. In Section 4 we discuss the importance of 3D modeling in

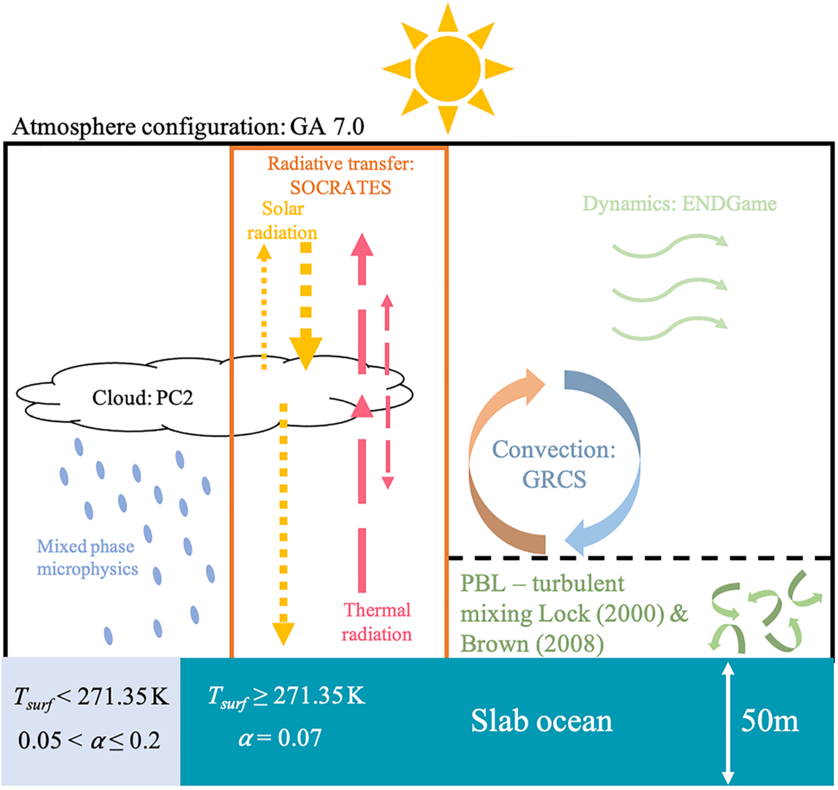

Figure 1. Schematic of the different components of the model. The GA 7.0 atmospheric configuration consists of the ENDGame dynamical core (Wood et al., 2014), the PC2 scheme to treat clouds (Wilson & Ballard, 1999; Wilson et al., 2008), microphysics is based on Wilson and Ballard (1999), SOCRATES to treat radiative transfer, the Gregory-Rowntree Convection Scheme (GRCS) (D. Gregory & Rowntree, 1990), with turbulent mixing in the planetary boundary layer (PBL) based on Lock et al. (2000) and A. R. Brown et al. (2008). The ocean is treated as a single layer slab of 50 m depth with no horizontal heat transport. Sea ice albedo is treated using Equation 1.

understanding the meridional circulation, and the possible impact haze may have on the results. Finally, we draw conclusions in Section 5 and highlight future avenues for improving on this study.

2. Modeling Framework

The UM has been used extensively to study the modern Earth (e.g., Andrews et al., 2020; Maher & Earnshaw, 2022; Sellar et al., 2019; Walters et al., 2019), and has been adapted to simulate a range of idealized Earth-like planets (e.g., Boutle et al., 2017, 2020; Eager-Nash et al., 2020; Lewis et al., 2018; Mayne et al., 2014; Sergeev et al., 2020; Sergeev et al., 2021; Yates et al., 2020). Here, we apply this model to the Archean, deep in the Earth's past. We use the Global Atmosphere (GA) 7.0 configuration (Walters et al., 2019). Dynamics are calculated using the ENDGame dynamical core (Wood et al., 2014), while convection is treated using a mass-flux approach based on D. Gregory and Rowntree (1990). Water clouds are treated using the prognostic cloud fraction and prognostic condensate scheme (PC2) (Wilson et al., 2008), which incorporates mixed phase microphysics based on Wilson and Ballard (1999). Turbulent mixing is based on Lock et al. (2000) and A. R. Brown et al. (2008). These schemes are combined and shown as a schematic in Figure 1. Simulations have a horizontal resolution of 2.5° in longitude by 2° in latitude, with 38 vertical levels between the surface ($z = 0$ km) and the top-of-atmosphere ($z = 40$ km) the same as that of Eager-Nash et al. (2020). The vertical levels are quadratically stretched to enhance the resolution at the surface.

The Suite of Community Radiative Transfer codes based on Edwards and Slingo (SOCRATES) scheme treats the radiative transfer in the UM, employing the correlated-k method (included in schematic in Figure 1). Thermal radiation is treated via 17 bands (between 3.3 μm and 10 mm), while solar radiation is treated by 43 bands (0.20–20 μm) using the `sp_lw_17_etw_arcc10bar` and `sp_sw_43_etw_arcc10bar_sun_2.9gya` spectral files respectively. These are suitable for atmospheres dominated by a mixture of N_2 and CO_2 (from 1% to 20%), with up to 3.5% CH_4 (tested in Appendix B), supporting surface pressures up to 10^6 Pa. These include CO_2 sub-Lorentzian line wings and CO_2 self-broadening. Collision induced absorption is included for: N_2–CH_4, N_2–N_2, and CO_2–CO_2 from HITRAN (Karman et al., 2019), and CH_4–CO_2 from Turbet et al. (2020). Line data are from HITRAN 2012 (Rothman et al., 2013), the same as used in Byrne and Goldblatt (2015). The solar spectrum is taken for a 2.9 Ga Sun spectrum from Claire et al. (2012). Testing of our radiative transfer against higher resolutions for the gas mixtures used here can be found in Appendix B and Figure B1, focusing on the CH_4 tropopause radiative forcing.

Methane radiative forcing is calculated at the tropopause. It is the net downward total "all-sky" radiative flux subtracted by the all-sky flux with methane switched off radiatively, which is calculated for the present model configuration without altering the climate state. Similar to the definition from the World Meteorological Organisation (1957), the tropopause is defined as the region above 500 hPa where the lapse rate is less than or equal to 2 K/km for at least two consecutive vertical model levels.

The simulations were configured as an aquaplanet, using a single layer slab homogeneous flat surface as the inner boundary (planet's surface), which is based on Frierson et al. (2006). It represents an ocean surface with a 50 m mixed layer with a heat capacity of 2.08×10^8 J/K/m^2, with no horizontal heat transport. The emissivity of the surface is fixed at 0.985 (Snyder et al., 1998) and the liquid water surface albedo (α_{sea}) is fixed at 0.07 (Jin et al., 2004). The assumption of an aquaplanet was made with predictions that the ocean water content may have been larger than today (Dong et al., 2021), and continental coverage was likely lower (Cawood et al., 2013). Although excluding horizontal heat transport in the ocean is inherently inaccurate, the uncertainty in continental coverage and location means that the inclusion of a dynamic ocean will also lead to further inaccuracies that may obfuscate the effects we are exploring in this work.

Sea ice albedo effect is represented by a change in albedo at 271.35 K ($T_{\mathrm{threshold}}$) using the HIRHAM parametrization from Liu et al. (2007), which calculates a temperature dependent sea ice albedo (α_{ice}) as

$$\boldsymbol{\alpha}_{\mathbf{ice}} = \boldsymbol{\alpha}_{\max} - \exp\left(-\frac{\boldsymbol{T}_{\mathbf{threshold}} - \boldsymbol{T}_{\mathbf{surf}}}{\mathbf{2}}\right) \times (\boldsymbol{\alpha}_{\max} - \boldsymbol{\alpha}_{\mathbf{sea}}), \tag{1}$$

where T_{surf} is the surface temperature and $\alpha_{\max}$ is the maximum sea ice albedo. A spectrally dependent $\alpha_{\max}$ is used following Joshi and Haberle (2012), which is independent of the spectral type of the host star. For spectral bands below 0.5 μm $\alpha_{\max} = 0.8$, while bands above 0.5 μm $\alpha_{\max} = 0.05$. If a bands range contains 0.5 μm the albedo of the band is a linear weighting of the two components. When convolved with the solar flux, in practice, our simplified scheme leads to a maximum ice albedo of approximately 0.2. Although this value is somewhat lower than expected, the simulations reproduced reasonable ice coverage for the modern Earth (not shown here). In reality, the scheme setup is compensating for missing heat transport via the ocean and the lack of a more sophisticated thermodynamic ice scheme, alongside sea ice transport. Simple non-thermodynamic ice schemes like the ones used here have been shown to result in larger climate fluctuations and generally less ice coverage than their thermodynamic counterparts (Poulsen & Jacob, 2004). Therefore, in our simulations we expect our approach to result in a smaller ice albedo feedback impact, subsequently making our simulations more resistant to entering a snowball state. In the future we will continue to develop the complexity and completeness of our model, but this often comes at a price of increased difficulty in understanding specific processes. Therefore, for this work, focused on the radiative impact of methane, we elected to use the simplified scheme described.

We focus our study on 2.7 Ga as at this time methane concentrations could have been high, as the evolution of oxygenic photosynthesis may have supported a widespread productive biosphere (indicated by depletion of organic carbon-13 in marine sediments, Eigenbrode & Freeman, 2006; Daines & Lenton, 2016). This increase in biotic oxygen production is prevented from oxidising the atmosphere by burial of oxidants in the highly insoluble form of iron oxides whilst reductant was added to the atmosphere as methane through recycling of organic carbon (Walker, 1987). Hence, there is a net oxidation of the Earth's surface and net reductant input into the atmosphere. Planetary parameters used in our simulations are presented in Table 1. The fainter Sun at 2.7 Ga meant that the solar constant was less than the present day. From Gough (1981) (their Equation 1), we can estimate this to be 81% of the modern solar constant, S_0, of 1361 W/m^2 (Kopp et al., 2016).

At 2.7 Ga the Earth's rotation rate was believed to be faster than the present Earth. Williams (2000) predict that the rotational period at 2.45 Ga could have been between 16.0 and 19.4 hr, while Bartlett and Stevenson (2016) (from their Figure 5) suggest a range of between approximately 16.0 to 19.5 hr at 2.7 Ga depending on the magnitude of the lunar torque at the time. In this study we use the value of 17 hr, although the exact value over this range has a minimal impact on the overall results presented here. For simplicity, the modern obliquity (see Table 1) is used as it is unclear how obliquity could be significantly different to the present day, however, following the choices made by Charnay et al. (2013), Wolf and Toon (2014), we set the eccentricity to zero.

Table 1
The Planetary and Orbital Parameters Used for All Planetary Configurations, Based on a 2.7 Ga Earth

Parameter	2.7 Ga Archean Earth
Stellar irradiance (W/m^2)	1,100.8 (0.809S_0)
Day length (hours)	17.0
Eccentricity	0
Obliquity (°)	23.44
pCO_2 (Pa)	100, 300, 1,000, 3,000
pCH_4 (Pa)	0, 1, 3, 10, 30, 100, 300, 1,000, 3,500
$pN_2 + pCO_2$ (Pa)	100,000
Surface pressure	$pN_2 + pCO_2 + pCH_4$

Note. Stellar irradiance is calculated using Gough (1981), based on a modern day solar constant $S_0 = 1361$ W/m^2 (Kopp et al., 2016). Rotation rate is based on estimates from Williams (2000) and Bartlett and Stevenson (2016). Partial pressures represent the values initialized in the model at the surface.

In these simulations, we vary the methane partial pressures from 1 to 3,500 Pa to cover the range predicted by Kharecha et al. (2005), as well as extending the lower limit in line with Byrne and Goldblatt (2015), to include potential methane concentrations from only abiotic sources, $pCH_4 \approx 1$ Pa (Kasting, 2005). We also include a baseline case, without methane, as a comparison for our simulations with varying atmospheric methane concentrations. We vary the initialized CO_2 surface partial pressure from 100 to 3,000 Pa covering some of the large variation in paleosol constraints (340–75,000 Pa) and use the lower value of 100 Pa to match Byrne and Goldblatt (2015). We vary pCO_2 to cover a range of predicted CO_2 abundances at the time, from 100 to 3,000 Pa. For $pCO_2 = 10{,}000$ Pa our simulations were significantly warmer than the modern day Earth and the UM becomes unstable for the higher methane concentrations. Therefore, we omitted these cases from our study and used $pCO_2 \leq 3{,}000$ Pa as the upper limit.

These surface partial pressures are the values initialized in the model, while the total surface pressure, and thus individual partial pressures, can evolve from the initialized value. However, the equivalent volume mixing ratios have no spatial or temporal variation. The reason for the choice in using partial pressures is to ensure that the mass of N_2 and CO_2 is kept constant with variations in CH_4 abundance. This is to replicate methane production by the biosphere, adding methane to the atmosphere. Surface pressures range from 1 to 1.035×10^5 Pa, which aligns with the upper limit of surface pressures from Som et al. (2012), as well as using similar conditions to Byrne and Goldblatt (2015).

Fixed gas mixing profiles are used in these simulations, with no chemistry included. This assumption is validated by 1D photochemical models, which show that the volume mixing ratio remains relatively constant up to 40 km (top of model in our simulations) for carbon dioxide (e.g., Huang et al., 2021) and methane (e.g., Kharecha et al., 2005; B. S. Gregory et al., 2021) at low oxygen concentrations.

Initial simulations with no CH_4 ran for 60 years to allow for atmospheric equilibrium to be reached. Subsequent runs with CH_4 present were initialized from these simulations and ran for another 50 years to reach a new steady state. All the simulations were in steady state by the final 15 years, so we use this period for our analysis. Steady state was deemed to have been reached when the top of atmosphere radiative flux was in balance and the mean global surface temperature was near constant. In this work, we refer to equatorial and polar regions. The equatorial region is considered as spanning latitudes of 10°S to 10°N, while the polar regions are 70°S/N to the pole, which are averaged over these regions in figures henceforth. UM output was processed and plotted using Python's IRIS (Met Office, 2010–2020), AELOUS (Sergeev & Zamyatina, 2022) and Matplotlib (Hunter, 2007) packages.

3. Results

In this section we demonstrate that methane has a maximum potential warming of up to 7 K globally in our Archean-like simulations. Furthermore, we find that the equator-to-pole temperature difference generally increases with pCH_4, which is driven by the difference in methane radiative forcing at the equator and poles and also the decrease in circulation strength driven by upper troposphere heating by methane shortwave absorption.

Methane radiative forcing plays an important role in driving the climate. This is shown for all of our simulations in Figure 2. Figure 2a shows the global tropopause radiative forcing by methane. As pCH_4 is increased, initially total radiative forcing increases due to an increase in longwave radiative forcing (dotted lines in Figure 2a) causing surface temperature to increase. As pCH_4 continues to increase, shortwave radiative forcing becomes more negative (dashed lines in Figure 2a) caused by absorption of shortwave radiation, which becomes comparable to the

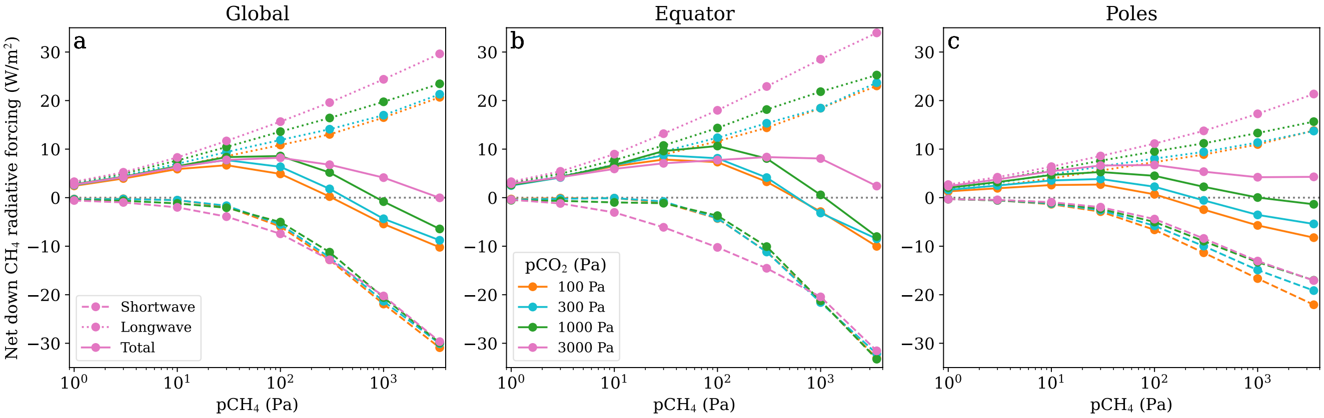

Figure 2. Panel (a) shows the global average net down radiative forcing at the tropopause for methane for shortwave (dashed), longwave (dotted) and their sum (solid). Panels (b and c) show the same as (a) averaged over 10°S to 10°N as the equator in (b), and poleward of 70°N/S for the polar regions in (c).

magnitude of longwave radiative forcing and causes methane's total radiative forcing to decrease again, driving a cooling of the surface. Similar to the results found in Byrne and Goldblatt (2014), the shortwave absorption becomes significant for $pCH_4 > 10$ Pa, with the total (longwave plus shortwave) methane radiative forcing similarly having a maximum of approximately 8.5 W/m^2, compared to 9 W/m^2 in Byrne and Goldblatt (2014).

Figures 2b and 2c show the methane radiative forcing for equatorial and polar regions respectively. Equatorial forcing exhibits similar trends to the global average, while polar radiative forcing is of a lower magnitude, with total radiative forcing peaking at smaller pCH_4 compared to the equatorial and global regions. Shortwave forcing is weaker at the poles for $pCO_2 = 3{,}000$ Pa compared to the other pCO_2 values, while longwave forcing is stronger, leading to methane radiative forcing at the poles plateauing at $pCH_4 \geq 1{,}000$ Pa.

The effects of this change in radiative forcing by methane are now explored for these different cases by examining the difference in climate between these configurations.

3.1. Meridional Air Temperature Variation and the Hadley Circulation

Increasing pCO_2 in our Archean-like configuration leads to a familiar result in increasing temperatures globally (e.g., Charnay et al., 2013). Figure 3 shows a subset of our simulations and reveals that increasing pCO_2 from 100 Pa to 3,000 Pa (comparing left and middle columns) at any pCH_4 leads to the zonal mean air temperatures rising globally in the troposphere, with the polar regions warming more than equatorial regions, shown by the right hand column of Figure 3, which shows the increase in air temperature from $pCO_2 = 100$ Pa to $pCO_2 = 3{,}000$ Pa. Minimum temperatures decrease due to the stratosphere cooling with increasing pCO_2 due to more efficient cooling of the atmosphere.

Increasing surface pCH_4 from 1 to 3,500 Pa, leads to a smaller change in troposphere air temperatures compared to changing pCO_2, but large increases in stratospheric temperature. Figure 3 shows that increasing pCH_4 initially leads to troposphere warming, which peaks between pCH_4 values of 30–300 Pa and increasing pCH_4 further leads to cooling of the troposphere at lower pCO_2 and plateauing at higher pCO_2 (see bottom row of Figure 3), which is driven by changes the methane radiative forcing (Figure 2a). Increasing pCH_4 also leads to a warming of the stratosphere, and the formation of a stratospheric temperature inversion, visible at $pCH_4 \geq 300$ Pa at $pCO_2 = 100$ Pa and $pCH_4 = 3{,}500$ Pa at $pCO_2 = 3{,}000$ Pa in Figure 3. The magnitude of the warming can by seen in bottom row of Figure 3, which shows the change in air temperature between $pCH_4 = 1$ Pa and $pCH_4 = 3{,}500$ Pa with the stratosphere warmer by up to 87 K at $pCH_4 = 3{,}500$ Pa and $pCO_2 = 100$ Pa. This warming of the stratosphere is caused by the increase in shortwave heating of the upper atmosphere caused by methane (shown by the contours in Figure 4). These changes in air temperature show similar trends to those presented in Byrne and Goldblatt (2015). Horizontally averaged pressure-temperature plots for the equator and poles are shown in Figure A4.

The Hadley circulation strength is shown in Figure 4 in the form of meridional stream functions. The shorter rotational period of the planet used here (17 hr day compared to 24 hr) leads to the Hadley circulation having a

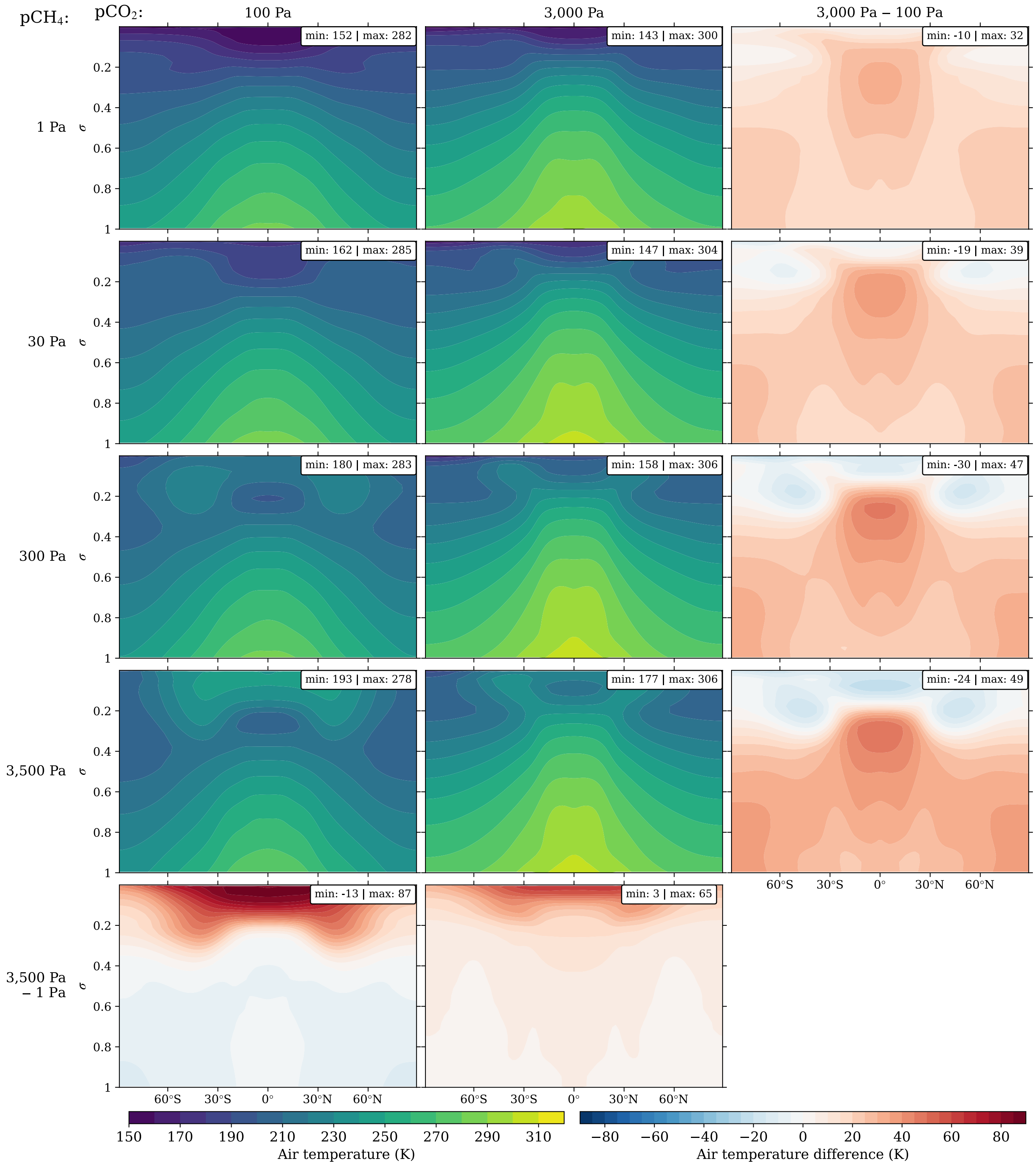

Figure 3. Zonal averaged air temperature (color scale), for increasing surface partial pressures of carbon dioxide from left to right, and methane from top to bottom. The right hand column shows the difference in air temperature between $pCO_2 = 100$ Pa and $pCO_2 = 3,000$ Pa (the left and middle columns). The bottom row shows the change in air temperature between the $pCH_4 = 1$ Pa and $pCH_4 = 3,500$ Pa case for a given pCO_2. In both of these cases a positive increase represents an increase in air temperature for the simulation with higher pCH_4/pCO_2. Plotted as latitude versus σ, where σ is the pressure divided by the surface pressure. This is for a subset of the simulations, with the full grid available in Appendix A (Figure A1). The same color scale is used for the left and middle columns, with maximum and minimum temperatures for each simulation displayed in the top right of each sub figure. The right column and bottom row use a another color scale that is constant between the subplots. These subplots also displays the maximum/minimum temperature differences in the top right of each sub figure.

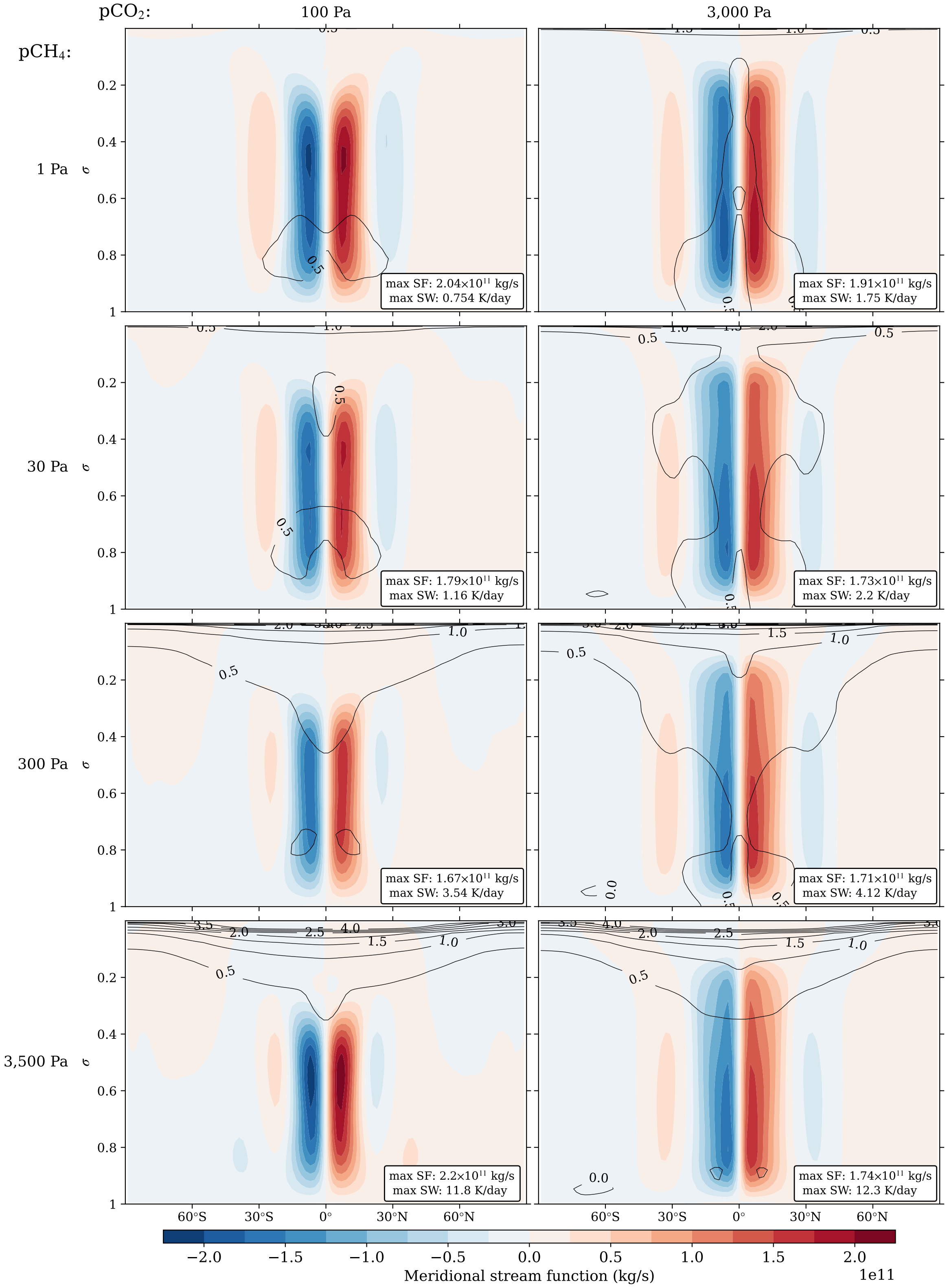

Figure 4. Zonal averaged meridional stream functions (color scale), for increasing surface partial pressures of carbon dioxide from left to right, and methane from top to bottom, in the same format as Figure 3, with the full grid available in Appendix A (Figure A2). Positive and negative values represent clockwise and anticlockwise circulation respectively. Contours show the heating of the atmosphere due to shortwave radiation in K/day. The same color scale is used for each plot, with maximum values for the stream function (SF) and shortwave heating rate (SW) are shown for each simulation in the bottom right of each sub figure.

reduced latitudinal depth, however there remains only three circulating cells. Additional cells are only expected to form at shorter rotational periods (Kaspi & Showman, 2015).

The latitudinal and vertical extent of the Hadley circulation increases when increasing pCO_2 as shown in Figure 4 (see Figure A2 for full grid of simulations). Increasing pCO_2 (left to right) leads to a stronger and deeper Hadley circulation, due to more efficient cooling of the upper tropopause and increasing surface temperatures increasing specific humidity. This is shown by the Hadley cells highlighted by the stream function intensifying, extending in latitudinal breadth and increasing the range of pressures they cover as pCO_2 is increased.

Increasing pCH_4 leads to a decrease in the latitudinal and vertical extent of the Hadley circulation, due to methane's shortwave heating of the upper troposphere for $pCO_2 < 3{,}000$ Pa, while at $pCO_2 = 3{,}000$ Pa the Hadley cell extent remains similar. For $pCO_2 = 100$ Pa, Figure 4 shows that at lower values of pCH_4 shortwave heating (black contour lines) predominantly takes place in the lower troposphere, while at higher pCH_4 the shortwave heating is largest in the upper troposphere. This is caused by high pCH_4 values increasing the shortwave absorption of the atmosphere. This results in the upper troposphere being more stable against convection at higher pCH_4, and reduces the tropopause height and subsequently the depth and strength of the Hadley circulation (also see lapse rates for a low pCO_2 and high pCH_4 case and a high pCO_2 and low pCH_4 in Figure A5). For $pCO_2 = 3{,}000$ Pa, efficient cooling of the upper troposphere by CO_2 counteracts methane heating in the stratosphere and upper troposphere (compare warming due to methane in the bottom two panels of Figure 3), allowing the vertical extent of the Hadley circulation to remain similar for all pCH_4 values.

3.2. The Global Effect of Methane on Climate

We now focus on the global effects of changing pCH_4 and pCO_2. In this section we demonstrate that methane has a maximum warming potential on the global mean surface temperature of less than 7 K for $pCO_2 \leq 3{,}000$ Pa for our 2.7 Ga Archean-like aquaplanet configuration (see Figure 5b). We compare these results to those of Byrne and Goldblatt (2015) who used a 1D RCM and find that our GCM simulations predict a stronger cooling effect at high methane concentrations.

The global mean surface temperature increase, caused by the addition of methane, is less than 7 K. Figure 5a shows the mean surface temperature for our simulated atmospheres without methane, that is, N_2 and CO_2 only with $pCH_4 = 0$, to act as a baseline for simulations where $pCH_4 > 0$. The subsequent temperature change from increasing pCH_4 is shown in Figure 5b. For our simulations the contribution of methane to the greenhouse effect peaks between pCH_4 values of 30–300 Pa, with peak global mean warming ranging from approximately 3.5 K to nearly 7 K as shown in Figure 5b. The location and magnitude of the peak in global mean surface temperature is dependent on pCO_2, with the peak occurring at higher pCH_4 and a larger maximum temperature as pCO_2 is increased. Past the peak, increasing pCH_4 leads to the global mean surface temperature decreasing, for which the decrease is largest for the lowest pCO_2, with some simulations for $pCO_2 \leq 1{,}000$ Pa globally cooler than the simulation with no methane at all (below gray dotted line in Figure 5b), with global mean surface temperature dropping by up to approximately 8 K at $pCH_4 = 3{,}500$ Pa compared to the maximum methane warming at constant pCO_2 (Figure 5b). This peaked response is caused by the balance between methane's longwave warming effect and its shortwave cooling effect, as discussed in Byrne and Goldblatt (2015) and presented here in Figure 2a.

Conversely, at the higher pCO_2 amount of 3,000 Pa, the decrease in surface temperature caused by $pCH_4 = 3{,}500$ Pa is minimal. From Figure 5c, it can be seen that the total water vapor and methane shortwave absorption increases less as pCH_4 increases for $pCO_2 = 3{,}000$ Pa compared to lower values of pCO_2. This is because the warmer climate at $pCO_2 = 3{,}000$ Pa allows for more water vapor in the atmosphere, which reduces the methane shortwave absorption due to overlap in their absorption cross sections in the shortwave. At higher pCO_2, the stratosphere becomes more resistant to the emergence of a stratospheric temperature inversion (see Byrne and Goldblatt (2015), Figure 3 and Figure A4), and at $pCO_2 = 3{,}000$ Pa, a cold trap only forms much deeper in the atmosphere (see Figure A4). This allows water vapor to reach higher abundances higher in the atmosphere, with stratospheric water vapor increasing significantly with pCH_4 for the $pCO_2 = 3{,}000$ Pa case only, shown in Figure 5d. This increase in stratospheric water vapor also acts to enhance the greenhouse effect, and leads to only a marginal drop in the global mean surface temperature for $pCO_2 = 3{,}000$ Pa in Figure 5b.

Use of a 3D GCM leads to a more significant global cooling at high pCH_4 (see Figure 5b) compared to results from a 1D RCM. $pCO_2 = 100$ Pa and $pCO_2 = 1{,}000$ Pa offer the most comparable configurations to Byrne

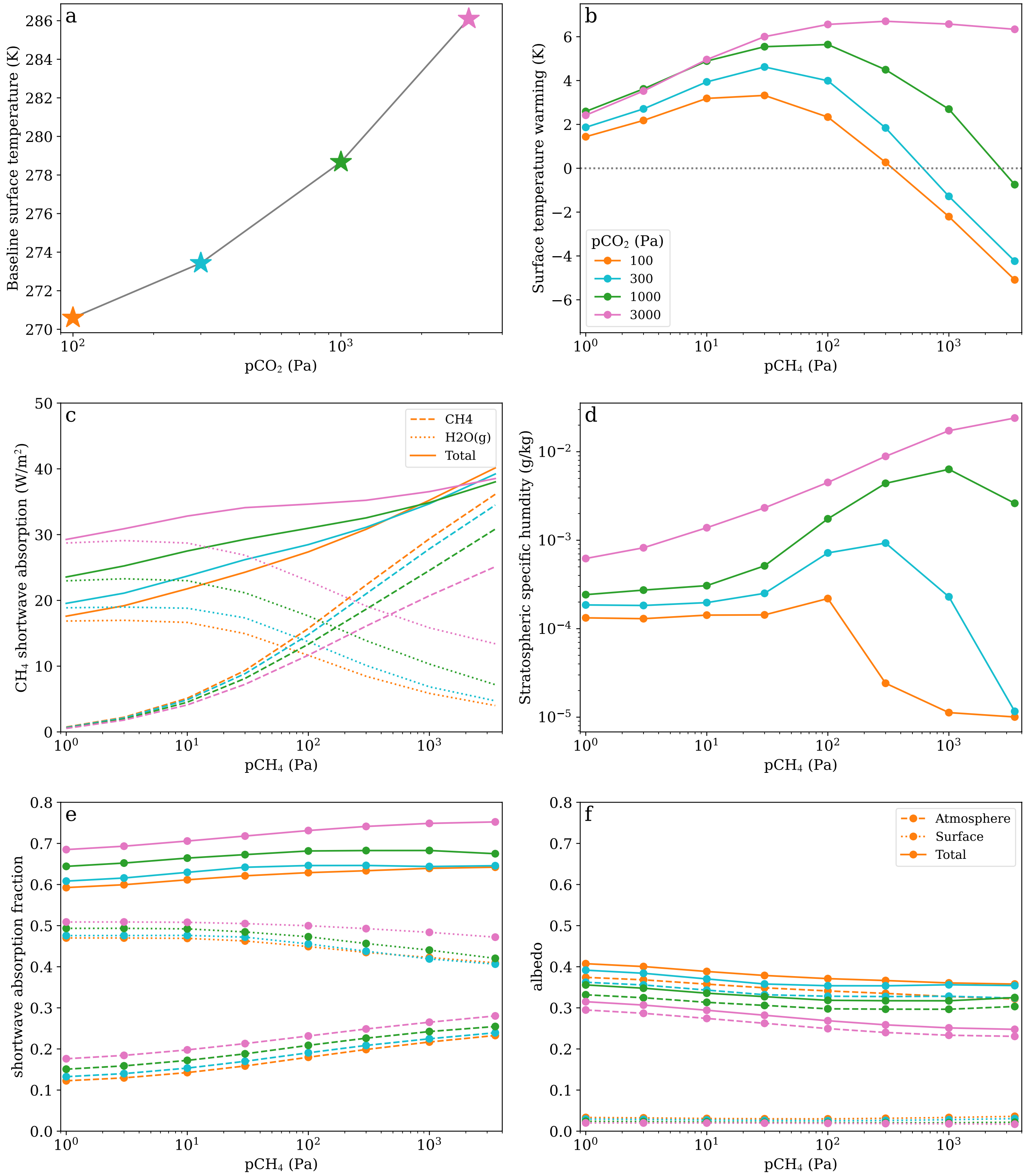

Figure 5. Panel (a) shows the global mean surface temperature with respect to the carbon dioxide concentration and assuming pCH$_4$ is zero, with (b) showing the subsequent change in global mean surface temperature due to the addition of pCH$_4$ (positive indicates warming). Colors of markers in (a) correspond to the same pCO$_2$ in (b). Similar plots for near surface specific humidity are shown in Figure A3. Panel (c) show the global average atmospheric absorption of shortwave radiation by methane (dashed) and water vapor (dotted) and their sum (solid). Panel (d) shows the specific humidity in the stratosphere at $\sigma = 0.1$. Panels (e and f) shows the fractional contribution of atmospheric (dashed), surface (dotted) and total (atmospheric plus surface) to the shortwave radiation budget global mean for shortwave absorption (e) and solar-weighted albedo (f). These were calculated using Donohoe and Battisti (2011), which accounted for atmospheric attenuation of shortwave radiation reflected by the surface.

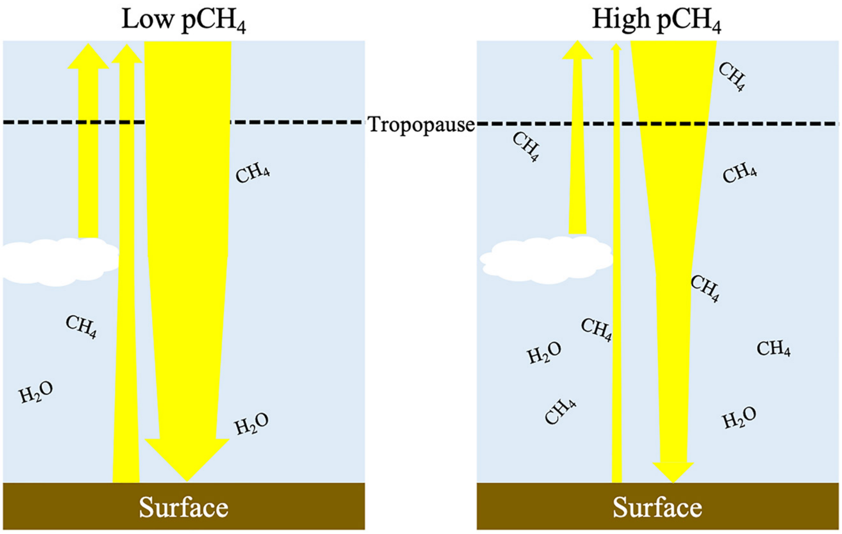

Figure 6. Schematic showing how methane affects the vertical distribution of shortwave radiation in the atmosphere for a low (left) and high (right) methane case. Shortwave radiation is represented by yellow arrows. A thinning of the arrow represents a loss of shortwave radiation through absorption in the atmosphere. Upward shortwave radiation represents reflected shortwave radiation from the surface and atmosphere. The tropopause is marked by a dashed line, and for simplicity is placed at the same level in these diagrams.

and Goldblatt (2015), who used CO_2 abundances of 10^{-3} and 10^{-2}. For a CO_2 abundance of 10^{-2}, Byrne and Goldblatt (2015) found a plateau in methane's greenhouse warming with surface temperature remaining constant up to a CH_4 abundance of 10^{-2} from 10^{-3}, compared to a ≈3 K drop in average surface temperature from the peak at $pCH_4 = 100$ Pa for $pCO_2 = 1{,}000$ Pa at $pCH_4 = 1{,}000$ Pa (temperature difference for green line between $pCH_4 = 100$ Pa to $pCH_4 = 1{,}000$ Pa in Figure 5b). Similarly for a CO_2 abundance of 10^{-3}, there is a cooling from the peak of ≈1 K in the 1D model compared to ≈5.5 K for $pCO_2 = 100$ Pa in our 3D model (temperature difference for orange line between $pCH_4 = 30$ Pa to $pCH_4 = 1{,}000$ Pa in Figure 5b). This increases to ≈8 K when $pCH_4 = 3{,}500$ Pa, however methane was not investigated at such levels in Byrne and Goldblatt (2015). These are caused, in part, by the presence of a 3D atmospheric circulation in the GCM, with methane affecting the meridional temperature gradient and Hadley circulation (see Section 3.3).

The addition of methane increases atmospheric shortwave absorption (Figure 5c) in the upper atmosphere and leads to a reduction in planetary albedo. Figure 5e shows this increase in atmospheric absorption of shortwave radiation with pCH_4. This leads to a decrease in surface shortwave absorption and a reduction in total albedo, shown in Figure 5f. As discussed in Section 3.1 as pCH_4 increases, shortwave heating transitions from predominantly heating the lower troposphere to heating the stratosphere and upper troposphere. This is caused by the increase in shortwave absorption higher in the atmosphere. This is summarized in the schematic in Figure 6.

The increase in shortwave absorption by methane higher in the atmosphere leads to a reduction in the water vapor shortwave absorption, shown in Figure 5c. This is due to spectral overlap between the absorption cross-sections of water vapor and methane in the shortwave (see Figure 6 in Byrne & Goldblatt, 2014). Increasing pCH_4 leads to an increase in shortwave radiation absorption high in the atmosphere by methane, where specific humidity is lower in concentration compared to lower in the troposphere (see Figure A4). However, the relative contributions to shortwave absorption by methane and water vapor also depends on the temperature, with warmer simulations having a higher specific humidity, leading to shortwave absorption higher in the atmosphere. This explains the greater rates of shortwave heating in the troposphere in Figure 4 for $pCO_2 = 3{,}000$ Pa (compared to $pCO_2 = 100$ Pa), which is significantly warmer than the other simulations. As a result, these simulations have less shortwave heating by methane at a given pCH_4 (compare magenta and orange dashed lines in Figure 5c).

3.3. The Effect of Methane on Equator-To-Pole Temperature Gradients

Although the global impacts of methane within our 3D GCM simulations qualitatively match the trends identified in Byrne and Goldblatt (2015), differences are apparent between the 1D and 3D results. In this section we describe the impacts of changing meridional transport across our simulations, which cannot be captured in 1D models. We find that the equator-to-pole temperature difference tends to increase with pCH_4 initially due to an increase in methane radiative forcing at the equator relative to the poles. As pCH_4 increases further, equator-to-pole temperature differences plateau due to an increase in radiative forcing at the poles and a decrease in efficiency in meridional heat transport.

The equator-to-pole temperature gradient reduces with increasing pCO_2, demonstrated in Figure 7a. This is due to an increase in the atmospheric temperature which increases the moist static energy transport (Kaspi & Showman, 2015). The meridional stream functions also increases in latitudinal and vertical extent, as shown in Figure 4. However, the meridional temperature gradient's response to methane is more complex.

Figure 7b shows the increase in equator-to-pole temperature difference as a result of the addition of methane to the simulations. From Figure 7b we find that increasing pCH_4 generally causes an increase in equator-to-pole temperature differences for $pCH_4 \leq 300$ Pa, above this the equator-to-pole temperature difference either begins to plateau or decreases. The exact change is dependent on the pCO_2, with the behavior more extreme for lower pCO_2, but the general trends remain. As well as this the main drivers for the meridional temperature gradients are methane's varying meridional radiative forcing (Figures 2b and 2c) and the effect on the meridional heat transport.

Figure 8a shows that for $pCO_2 \leq 1{,}000$ Pa increasing pCH_4 initially leads to an increase in the relative CH_4 tropopause forcing at the equator compared to the pole, which drives an increase in the equator to pole temperature difference. This suggests, that for $pCH_4 \leq 300$ Pa, the equator-to-pole temperature difference in Figure 7b is driven by the differences in CH_4 radiative forcing.

The plateau that emerges in the equator-to-pole temperature differences in Figure 7b as pCH_4 increases above 300 Pa, can be explained by a balance between a weakening of the meridional heat transport and an increase in methane radiative forcing at the poles relative to the equator. For $pCO_2 \leq 1{,}000$ Pa, as pCH_4 increases above 100 Pa, the difference in the equator-to-pole radiative forcing decreases in Figure 8a, with polar forcing approaching equality to the equatorial radiative forcing and eventually exceeding it at $pCH_4 = 3{,}500$ Pa. However the change in equator-to-pole temperature differences over this period shows only a small (order of 2 K between 300 and 3,500 Pa) generally increasing trend compared to the large increase in the relative methane radiative forcing between the equator and pole (Figure 8a), which would work to decrease the equator-to-pole temperature difference. The minimal change in the equator-to-pole temperature difference is caused by a reduction in the meridional heat transport, which offsets the increase in methane radiative forcing at the poles relative to the equator. Meridional heat transport weakens due to a reduction in the latitudinal extent of the Hadley circulation (Figure 4) and a reduction in global mean surface temperature compared to the peak in Figure 5b, which would act to increase equator-to-pole temperature differences (see Figure 8b). This balance maintains a relatively small change in equator-to-pole temperature differences for $pCH_4 \geq 300$ Pa in Figure 7b.

At $pCO_2 = 3{,}000$ Pa, the equator-to-pole temperature difference change is smaller compared to the other case, changing by ≈6 K in total from $pCH_4 = 1$ Pa to $pCH_4 = 3{,}500$ Pa. This is partly due to the latitudinal extent of the Hadley circulation in Figure 4 remaining similar at $pCO_2 = 3{,}000$ Pa, which may be more important in controlling equator-to-pole temperature difference compared to the change in radiative forcing between the equator and poles. For $pCH_4 \leq 30$ Pa and $pCO_2 = 3{,}000$ Pa relative radiative forcing between the equator and poles remains constant (Figure 8a). At $pCO_2 = 3{,}000$ Pa for $pCH_4 > 30$ Pa equatorial forcing increases relative to the poles, with the equator-to-pole temperature difference increasing. The reduction in temperature difference between $pCH_4 = 1{,}000$ Pa and $pCH_4 = 3{,}500$ Pa may be partially driven by larger methane radiative forcing at the poles compared to the equator at $pCH_4 = 3{,}500$ Pa.

A reduction in the meridional heat transport with increasing pCH_4 above 30 Pa contributes toward an increase in the equator-to-pole temperature gradient. As discussed in Section 3.1 the Hadley circulation reduces in vertical and latitudinal extent when increasing pCH_4 (see Figure 4). The effect this has on the atmospheric heat transport for the equatorial and polar regions is shown in Figures 7c–7f. We used the net flux difference between the surface and top of atmosphere to estimate the flux transported horizontally into a region, as described in Lambert et al. (2011) (see Appendix C for more detail), and shown for our simulations in Figures 7c–7f. The change in heat flux out of the equator is relatively small compared to the poles, with changes on order of less than 5% due to changes in methane (by comparing Figures 7c and 7d). Figure 7f shows that as pCH_4 increases, there is an

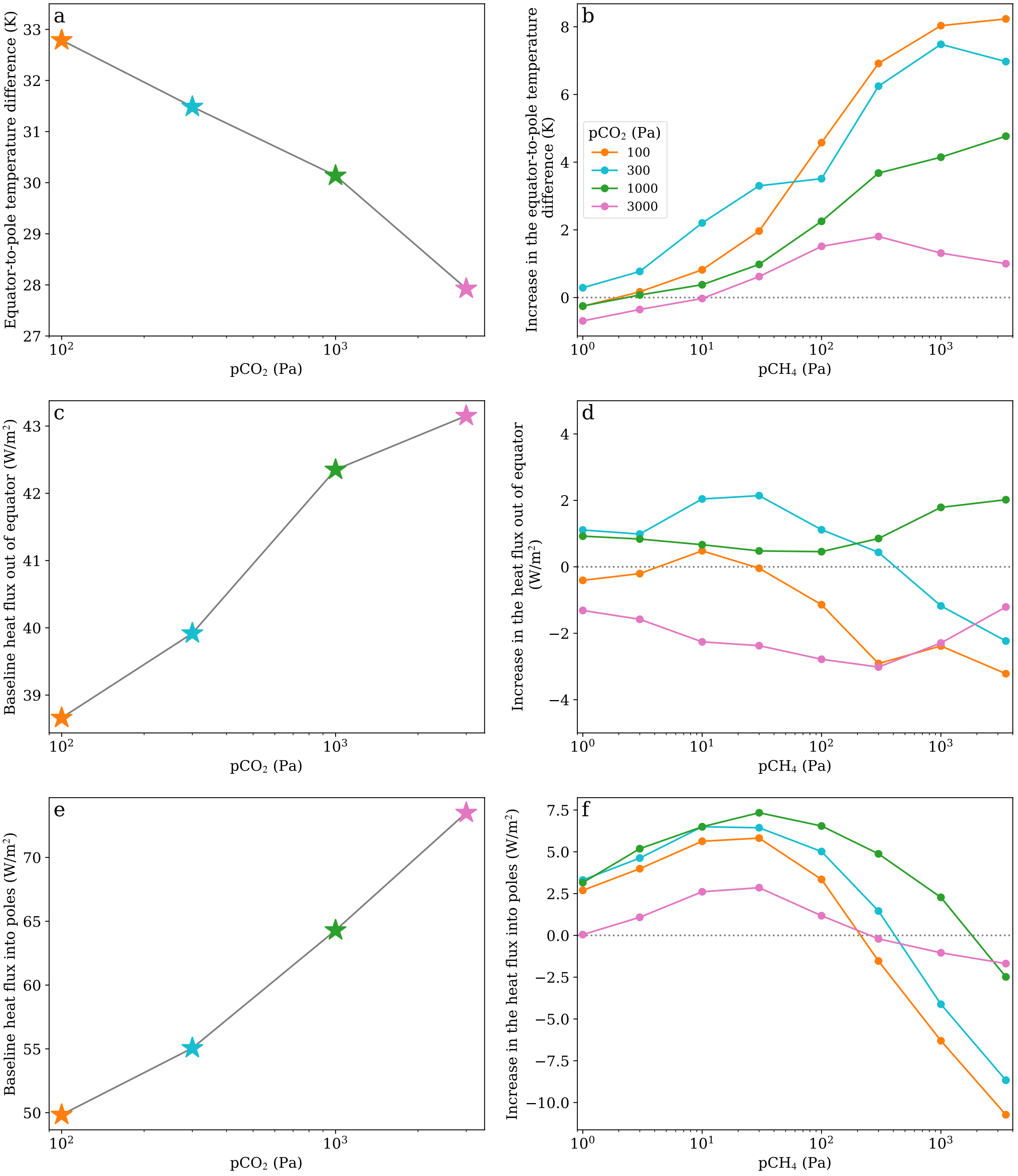

Figure 7. Panel (a) shows the average equator-to-pole temperature difference with only carbon dioxide (pCH$_4$ = 0), with (b) showing the subsequent increase in equator-to-pole temperature difference due to the addition of methane (positive indicates an increase in the equator-to-pole temperature difference). Panel (c) shows the atmospheric heat flux out of the equatorial region for different pCO$_2$ with pCH$_4$ = 0 (referred to as baseline cases), while panel (d) shows the increase in the equatorial heat flux from the subsequent addition of methane to (c). Panel (e) shows the atmospheric heat flux into the polar regions for different pCO$_2$ (with pCH$_4$ = 0), while (f) shows the increase in the polar heat flux from the subsequent addition of methane to (e). Calculations for (c–f) use methods from Lambert et al. (2011) to calculate atmospheric heat fluxes (see Appendix C for more detail). The equatorial region is considered as spanning latitudes of 10°S to 10°N, while the polar regions are 70°S/N to the pole. Colors of data points in panel (a, c, and d) correspond to the same pCO$_2$ in (b, d, and f).

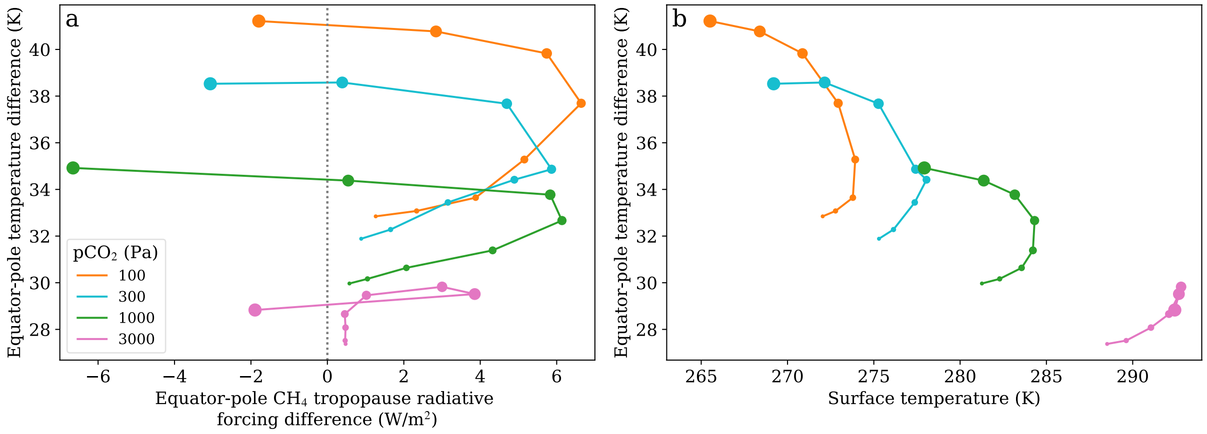

Figure 8. (a) Shows the equator-to-pole temperature difference against the difference in equatorial and polar net downward pCH_4 tropopause radiative forcing (positive indicates an increase in radiative forcing at the equator relative to the poles). Panel (b) shows the global mean surface temperature against the equator-to-pole temperature difference. The equatorial region is considered as spanning latitudes of 10°S to 10°N, while the polar regions are 70°S/N to the pole. pCH_4 is represented through the size of the marker (larger maker equivalent to a higher pCH_4) for pCH_4 values of {1, 3, 10, 30, 100, 300, 1,000, 3,500} Pa.

initial increase in heat flux into the poles, which peaks at $pCH_4 \approx 30$ Pa, potentially a result of the warmer global temperatures increasing the energy transported into the poles through moisture. Above $pCH_4 \approx 30$ Pa heat flux into poles reduces again, which is expected from the weakening circulation in Figure 4, and a corresponding sharp decrease in polar heat flux can be seen with a corresponding sharp rise in the equator-to-pole temperature difference (shown in Figure 7b). The equator-to-pole temperature difference's response to increasing pCH_4 is also dependent on pCO_2, as shown in Figure 7b.

The enhanced longwave forcing by methane at higher pCO_2 values in Figure 2 is due to an increasing temperature contrast between the surface and upper troposphere. Figure 9 shows this change in temperature contrast for the polar regions. The temperature contrast increases with pCO_2, leading to the increased longwave forcing seen in Figures 2a–2c. In contrast, methane acts to warm the stratosphere and upper troposphere by absorbing solar radiation and thus increasing methane decreases the temperature contrast, shown in Figure 9.

For this study clouds play only a secondary effect, and are not, therefore, discussed in detail. Figure 10 shows the cloud radiative effect at the tropopause, and although the magnitude of the change in longwave and shortwave cloud radiative effect vary the total cloud radiative effect remains nearly constant. Cloud fractions horizontally averaged pressure-temperature plots for the equator and poles are shown in Figure A4. We are currently working on a more in-depth study of the impacts of clouds over this parameter space.

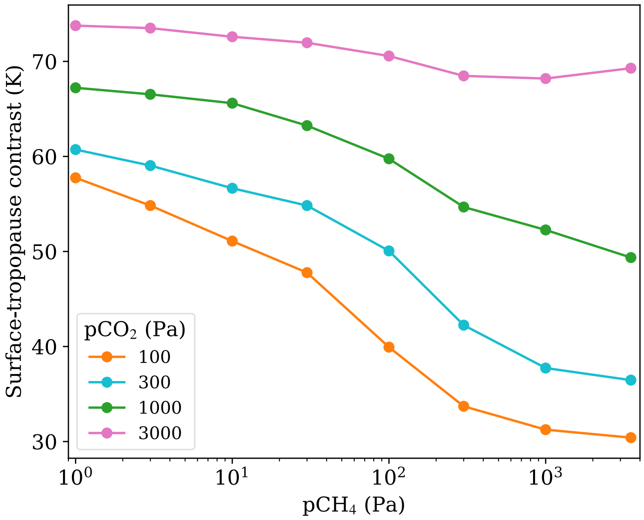

Figure 9. Shows the temperature contrast between the surface and atmosphere at $\sigma = 0.2$ horizontally averaged over the polar regions. The poles span from 70°N/S to the pole. $\sigma = 0.2$ is used to approximate the tropopause height.

4. Discussion

GCMs provide useful insight into the role of methane in the Archean climate, both validating effects found in RCMs and also finding important differences that come from 3D modeling. The initial global warming due to methane is similar between both models, with the models diverging when predicting temperatures for $pCH_4{:}pCO_2 > 0.1$. In this range GCMs predict large temperature drops, particularly for cooler, lower CO_2 configurations, with temperatures dropping by up to 8 K from the peak temperature.

GCMs are also useful in their ability to investigate the meridional heat distribution, where methane plays three important roles. (a) Differences in equator-to-pole methane radiative forcing: equator dominated for $pCH_4{:}pCO_2 < 0.1$, and transitioning to polar dominated above this. (b) Hadley circulation weakens when increasing pCH_4, which reduces meridional heat transport. (c) Atmospheric temperatures affect the moisture held in the atmosphere, so the peaking in temperature at $pCH_4{:}pCO_2 = 0.1$ leads to

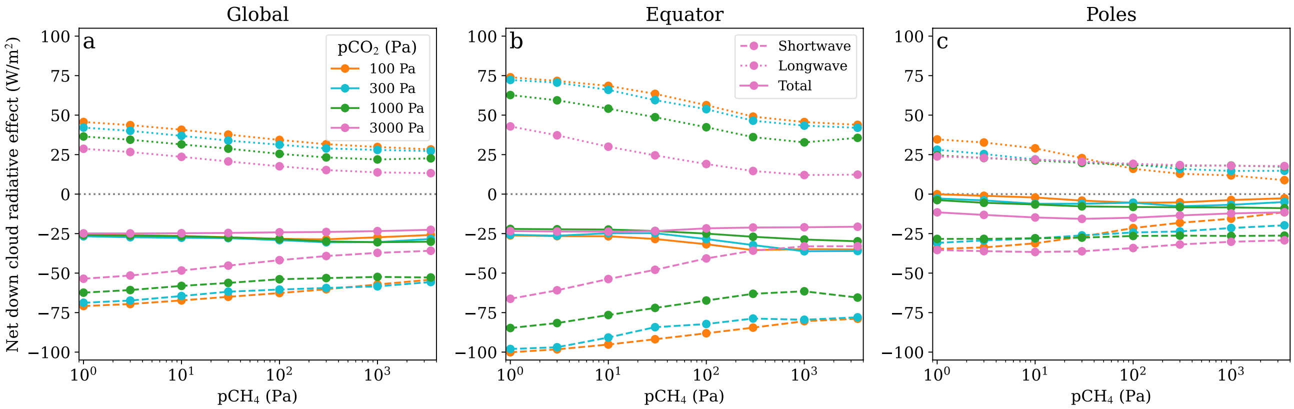

Figure 10. Panel (a) shows the global average net down cloud radiative effect at $\sigma = 0.2$ (approximate location of the tropopause) where σ is the pressure divided by the global mean surface pressure. Cloud radiative effect is shown for shortwave (dashed), longwave (dotted) and their sum (solid). Panels (b and c) show the same as (a) averaged over 10°S to 10°N as the equator in (b), and poleward of 70°N/S for the polar regions in (c).

increases in meridional heat transport below this and decreasing heat transport above this when increasing pCH_4. It may be possible to replicate this in a 2 column model (equatorial and polar column) by parameterizing these three factors.

Our study supports that the FYS paradox can be resolved based on pCO_2 constraints around 2.7 Ga. Global mean surface temperatures close to the pre-industrial Earth, can be achieved with $pCO_2 = 3{,}000$ Pa and $pCH_4 = 0$ Pa and $pCO_2 = 1{,}000$ Pa and $pCH_4 \approx 100$ Pa (Figures 5a and 5b). The first of these falls within the range of pCO_2 values constrained by Kanzaki and Murakami (2015) from 2.75 Ga, while the latter composition falls within the constraint of Driese et al. (2011) at 2.7 Ga. The addition of methane to $pCO_2 = 3{,}000$ Pa up to $pCH_4 = 3{,}500$ Pa would lead to global mean surface temperatures up to 7 K warmer than the pre-industrial Earth, while increasing or decreasing methane from the $pCO_2 = 1{,}000$ Pa and $pCH_4 \approx 100$ Pa configuration would lead to global mean temperatures decreasing. For $pCO_2 = 300$ Pa and $pCO_2 = 100$ Pa, global mean temperatures could reach up to 278 and 274 K respectively, with optimal methane abundances. In our simulations, these remain ice free, with Wolf and Toon (2013) finding that these concentrations of CO_2 with some CH_4 also avoid being fully glaciated, with at least 50% of the surface remaining ice free. Higher pCO_2 values than 3,000 Pa are not necessary for surface pressures around 10^5 Pa, but could be important to warm the Archean Earth if the total surface pressure was lower.

Some studies have suggested that surface pressures may have been lower than the present day. Fossil raindrops have been used to approximate surface pressure at 2.7 Ga to between 5×10^4 and 1.1×10^5 Pa (Som et al., 2012), although debate remains over the upper limit of this constraint (Kavanagh & Goldblatt, 2015). Furthermore, fossilized gas bubbles in lava flows at 2.74 Ga predict a surface pressure of $2.3 \pm 2.3 \times 10^4$ Pa (Som et al., 2016). The understanding of the effect of methane on the climate at different pressures is thus very important for the Archean, to be considered in future studies.

Methane has a secondary impact on the climate through its importance in the formation of hydrocarbon hazes, and it is suggested that there may have been periods during the Archean where a haze layer was present (Domagal-Goldman et al., 2008; Izon et al., 2015). Haze forms when the CH_4:CO_2 ratio exceeds approximately 0.1 (Trainer et al., 2006), and potentially has a cooling effect on climate by up to 20 K (Arney et al., 2016). Arney et al. (2016) found that a thick haze was produced for pCH_4:$pCO_2 > 0.2$. For $0.1 < pCH_4$:$pCO_2 < 0.2$ a thin haze is produced that is spectrally indistinguishable from an atmosphere with no haze (Arney et al., 2016). The peak surface temperature in our experiments were found to occur around $pCH_4/pCO_2 > 0.1$ so we expect this peak to remain with the presence of haze, and for $pCH_4/pCO_2 > 0.2$ hazes form and accelerate cooling further. Although we intend to study hazes in future work, with global mean surface temperatures for a given pCO_2 tending to peak around $pCH_4 = 0.1 \times pCO_2$, higher methane concentrations are not able to increases global mean surface temperatures further, even without considering the effects of haze.

Byrom and Shine (2022) and Collins et al. (2018) found that surface albedo can affect the shortwave radiative forcing, with higher albedos at wavelengths where methane absorbs strongly leading to an increase in absorption of upward radiation leading to a positive radiative forcing, which can arise from high albedo on land surfaces such as deserts (Byrom & Shine, 2022). Land fraction remains uncertain for the Archean (see discussion in Charnay et al., 2020), with a general consensus that the fraction of continental crust was less than present day (Hawkesworth et al., 2019), as well as the potential for a larger ocean volume (Dong et al., 2021), with suggestions land fraction could have been as low as 2%–3% until 2.5 Ga (Flament et al., 2008). We test the sensitivity of the tropopause radiative forcing by increasing global ocean albedo to 0.533 (value for albedo of quartz sand in near infrared, used in Byrom and Shine (2022)) and run the model for one time step and compare the radiative forcings, shown in Appendix D. Using this extreme value for albedo, we find that the shortwave radiative forcing becomes less negative. However the general trend for radiative forcing remains the same. Thus, for a surface with higher albedo, we would expect the decline in global mean surface temperatures to be less at higher methane values. Further exploration is required to explore the effect of different continent configurations on the methane radiative forcing and the overall effect on climate, with a spectrally dependent surface albedo.

Although methane, across the range we have studied, has a relatively small effect on global mean surface temperatures of −6 to +7 K, its abundance has a more significant impact on the meridional heat transport, which could affect the likelihood of the planet entering a snowball state. High methane levels generally increase the equator-to-pole difference by up to 8 K, which combined with a realistic ice-albedo feedback could affect the stability of the temperate state—which in this case refers to a state that is not fully glaciated. However full understanding of this would require consideration of ocean heat transport, continental configuration and a thermodynamic treatment of sea-ice, all of which are beyond the scope of this study, which focuses on the climate differences stemming from methane's radiative effect.

Theoretical opacity data that further fill in missing regions of methane's shortwave absorption up to 833 nm (Yurchenko & Tennyson, 2014) and 746 nm (Hargreaves et al., 2020) have also become available that allows for further investigation into the significance of methane's shortwave absorption. However, line lists for methane covering much of the wavelength region covered by the Sun's emission are not yet available, motivating the extension of work generating line lists to cover this missing absorption data.

Potentially habitable planets have now been detected orbiting M-dwarf stars, which are cooler than the Sun. For these exoplanets the shortwave absorption would be stronger due to a larger fraction of the stellar emission coming from the near infrared, for M-dwarfs compared to G-dwarfs like the Sun, where methane has strong absorption. The impacts of missing absorption data, as discussed above, become even more important due to the host star emitting more radiation at longer wavelengths where absorption from greenhouse gases is higher (Eager-Nash et al., 2020). If these planets host life, their early environment may have resembled that of the Archean Earth, given that a significant fraction of Earth's own "inhabited" history is represented by this period (Catling & Zahnle, 2020). Therefore, these planets could have high concentrations of methane and an even stronger temperature sensitivity to methane abundance due to the interaction of the host star spectrum and the methane rich atmosphere.

5. Conclusions

We used the Met Office Unified Model to understand the potential effect of atmospheric CH_4 and CO_2 on the climate of the Archean at 2.7 Ga. A productive biosphere could have led to an atmosphere with pCH_4 ranging from 10 to 3,500 Pa (Kharecha et al., 2005). We found that the greenhouse effect of methane does not exceed a global average of 7 K for $pCO_2 \leq 3{,}000$ Pa, with the peak temperature occurring for pCH_4 between 30 and 300 Pa. This peak in temperature shifts to higher pCH_4 for higher values of pCO_2. The peaked effect is due to methane's absorption of shortwave radiation in the stratosphere that reduces heating of the surface, which dominates over the greenhouse effect of methane at higher pCH_4. We confirm results from Byrne and Goldblatt (2015) and extend them to 3D simulations, but also demonstrate that use of a 3D GCM is important to fully capture cooling of the climate at high methane concentrations, due to changes in meridional circulation and methane radiative forcing. Maximum temperatures are reached when the CH_4:CO_2 is approximately 0.1, below the ratio where significant cooling occurs due to the presence of haze (Arney et al., 2016). More work is required to understand the interaction of biogeochemical cycles with the atmospheric composition and potential haze formation.

Appendix A: Additional Figures

Here, we present results from all of our simulations for cases matching figures in the main paper, as well as additional figures relating to specific humidity, clouds and lapse rate. Figure A1 and Figure A2 shows the same

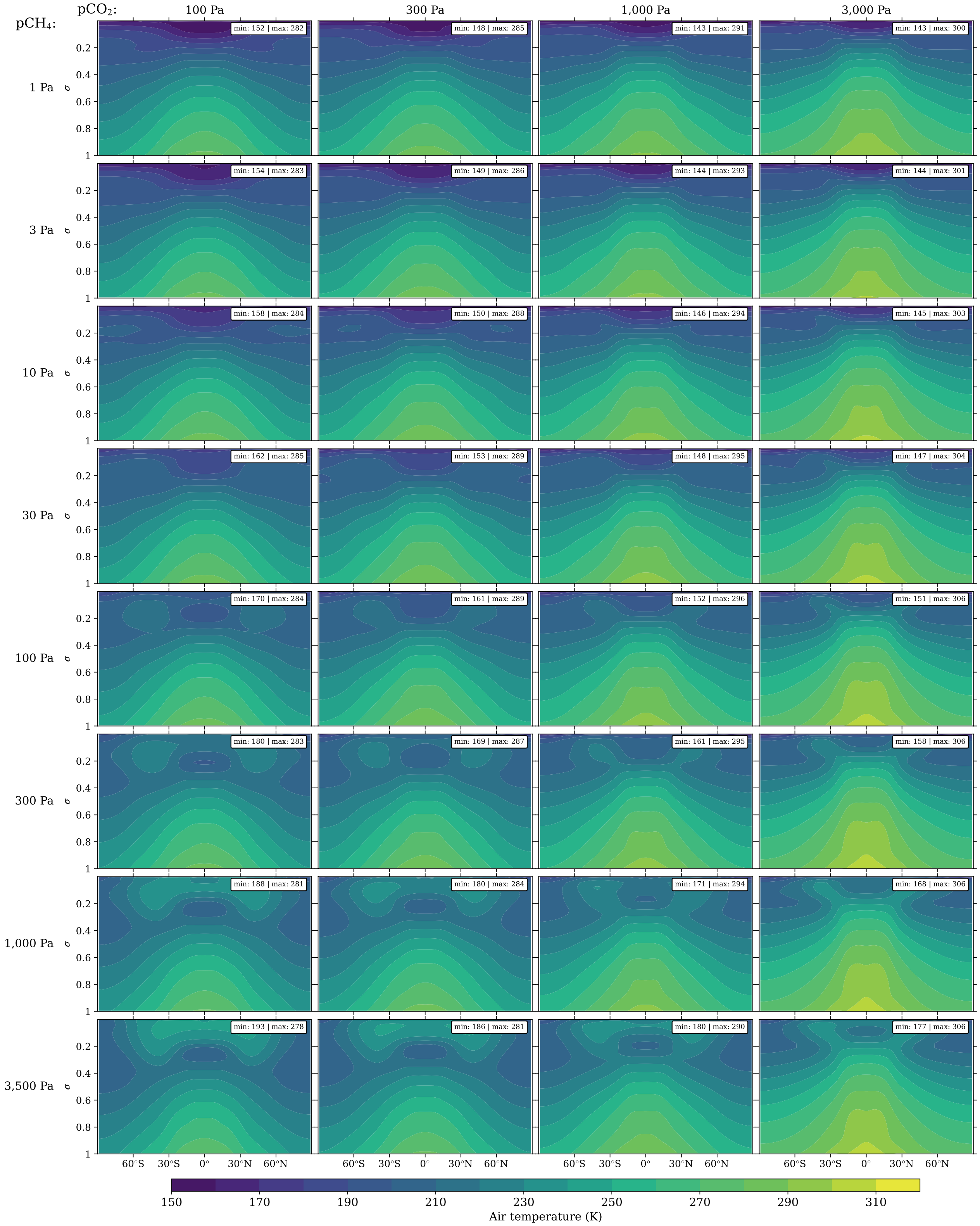

Figure A1. Zonal averaged air temperature (color scale), for increasing surface partial pressures of carbon dioxide from left to right, and methane from top to bottom. Plotted as latitude versus σ, where σ is the pressure divided by the global mean surface pressure. The same color scale is used for each plot, with maximum and minimum temperatures for each simulation displayed in the top right of each sub figure.

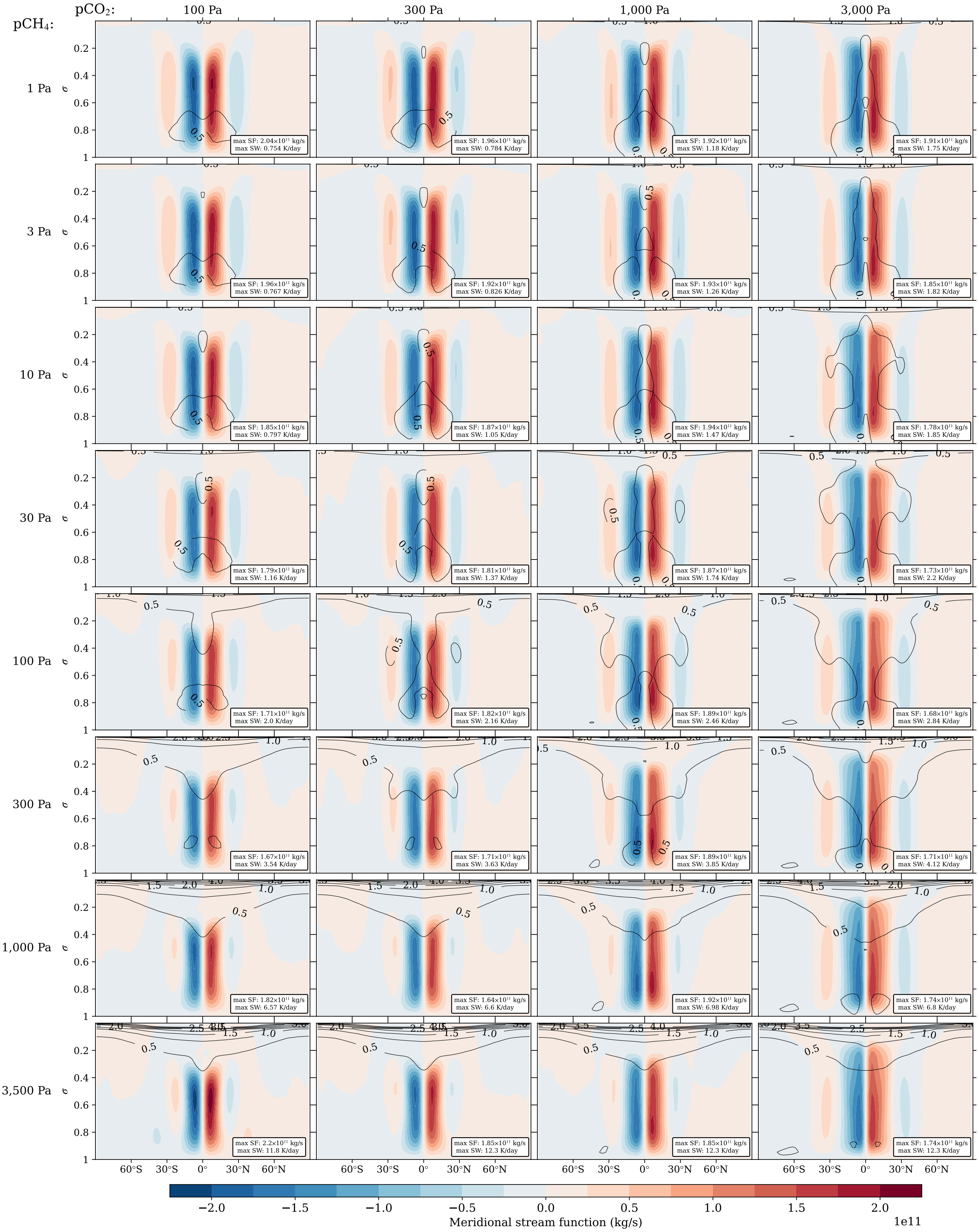

Figure A2. Zonal averaged meridional stream functions (color scale), for increasing surface partial pressures of carbon dioxide from left to right, and methane from top to bottom. Positive and negative values represent clockwise and anticlockwise circulation respectively. Contours show the heating of the atmosphere due to shortwave radiation in K/day. The same color scale is used for each plot, with maximum values for the stream function (SF) and shortwave heating rate (SW) are shown for each simulation in the bottom right of each sub figure.

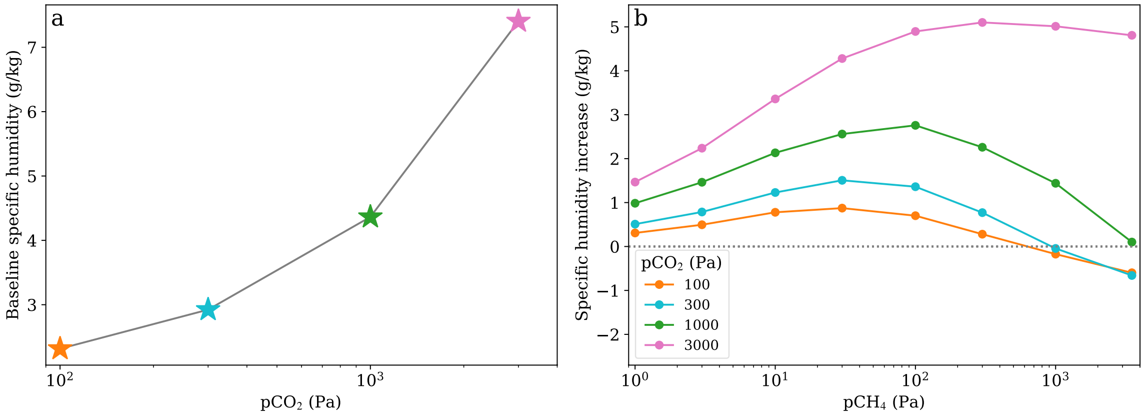

Figure A3. Similar to Figure 5 (a) shows the global mean near surface ($\sigma = 1.0$) specific humidity with respect to the carbon dioxide concentration and assuming pCH_4 is zero, with (b) showing the subsequent change in global mean near surface specific humidity due to the addition of pCH_4 (positive indicates warming). Colors of markers in (a) correspond to the same pCO_2 in panel (b).

information as Figures 3 and 4 respectively, but for the full grid of simulations. Figure A3 shows the global mean near surface specific humidity change for different pCO_2 and pCH_4 values, similar to Figures 5a and 5b. Figure A4 show air temperature, specific humidity and cloud area fractions to supplement data presented in Figure 5, Figures 2 and 9. Figure A5 shows the lapse rate for a low CO_2 and high CH_4 case (pCO_2 = 100 Pa, pCH_4 = 3,500 Pa) and a high CO_2 and low CH_4 case (pCO_2 = 3,000 Pa, pCH_4 = 1 Pa).

10.1029/2022JD037544

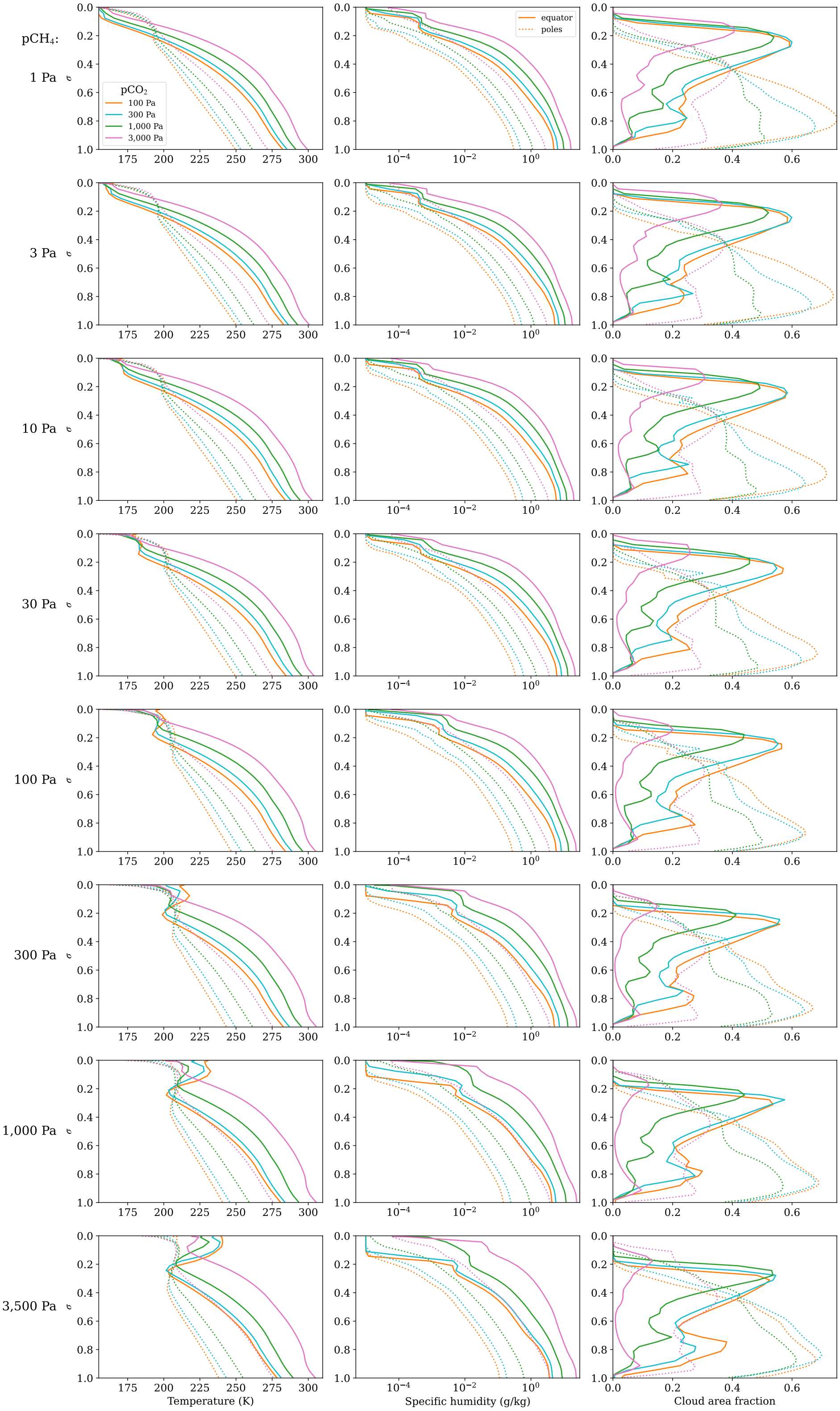

Figure A4. Shows horizontally averaged air temperature (left column), specific humidity (middle column) and cloud area fraction (right column) for the equator (solid lines) and poles (dotted lines), for increasing surface partial pressures of methane from top to bottom. The equator is considered as spanning latitudes of 10°S to 10°N, while the poles are 70°S/N to the pole.

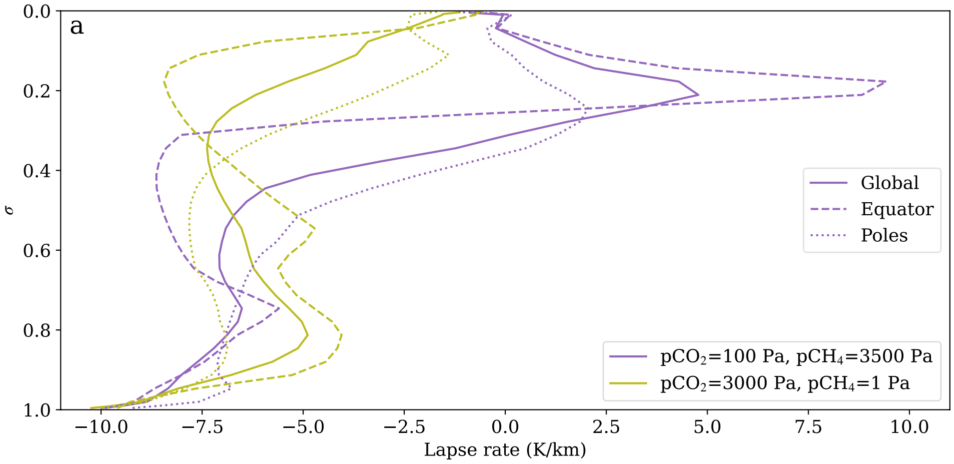

Figure A5. Shows lapse rate for the global (solid lines), equatorial (dashed lines) and polar (dotted lines) averages, for $pCO_2 = 100$ Pa and $pCH_4 = 3{,}500$ Pa (purple) and $pCO_2 = 3{,}000$ Pa and $pCH_4 = 1$ Pa (green). The equator is considered as spanning latitudes of 10°S to 10°N, while the poles are 70°S/N to the pole.

Appendix B: Spectral Resolution Sensitivity Analysis

Here, we make comparisons between spectral resolutions used in this study and a higher resolution spectral file treatment with 280 solar radiation bands (`sp_sw_280_etw_arcc10bar_sun_2.9gya`) and 350 thermal radiation bands (`sp_lw_350_etw_arcc10bar`) to assess the accuracy of our radiative transfer calculation. The results of this are shown in Figure B1. Errors in both the shortwave and longwave forcing remain small compared to the trends observed in Figure 2, and thus will not affect the overall results.

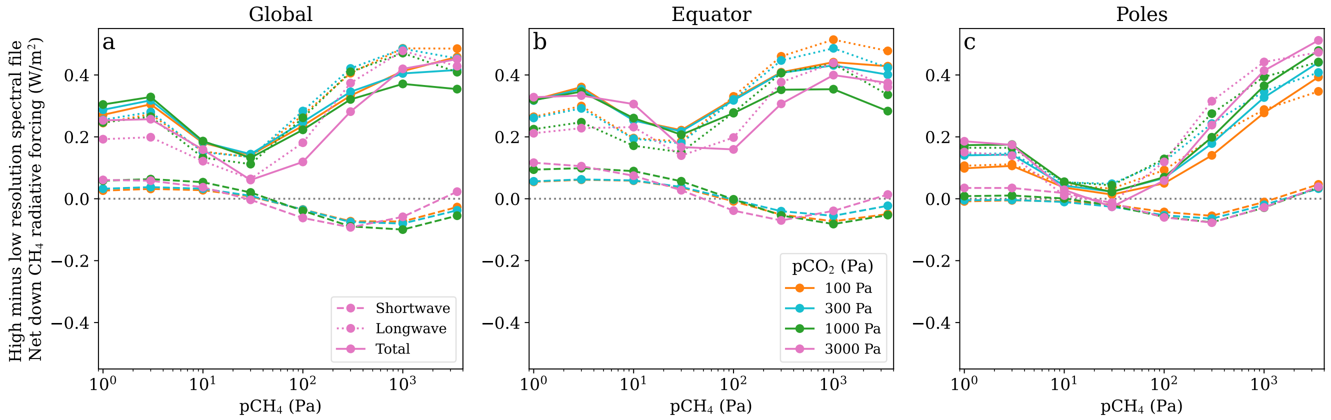

Figure B1. Panel (a) shows the high resolution minus the low resolution spectral file global average net down radiative forcing at the tropopause for methane for shortwave (dashed), longwave (dotted) and their sum (solid). Panels (b) and (c) show the same as (a) averaged over 10°S to 10°N as the equator in (b), and poleward of 70°N/S for the polar regions in (c). The high resolution spectral files for thermal and solar radiation are `sp_lw_350_etw_arcc10bar` and `sp_sw_280_etw_arcc10bar_sun_2.9gya` respectively, while the low resolution spectral files are `sp_lw_17_etw_arcc10bar` and `sp_sw_43_etw_arcc10bar_sun_2.9gya` for thermal and solar radiation respectively.

Appendix C: Calculations of Heat Fluxes in Polar and Equatorial Regions

Here, we outline the method used by Lambert et al. (2011) to understand the net heat transport in and out of regions of the atmosphere. This method was initially designed for use in understanding heat transport by the atmosphere between regions of the atmosphere covering land and ocean. Here, we apply this to heat transport out of equatorial regions and into polar regions, with the heat flux out of the equatorial region, $\frac{\Delta A_E}{f_E}$, given as:

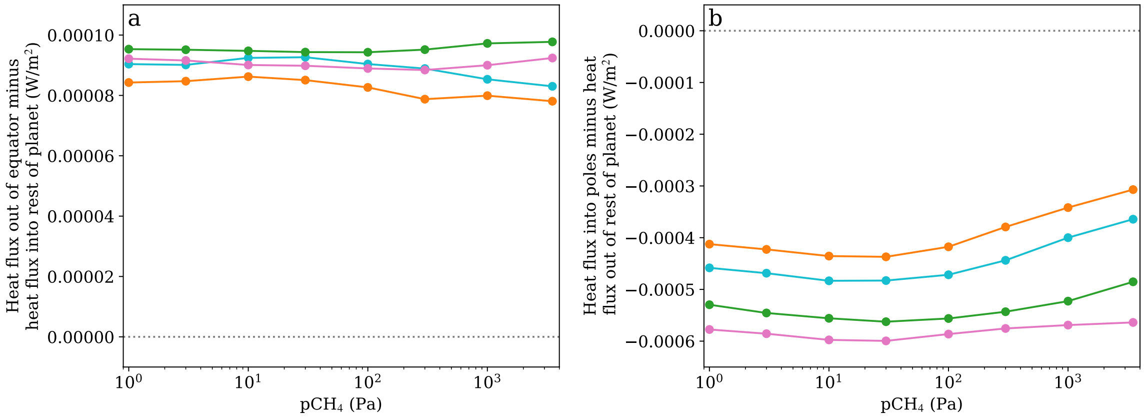

Figure C1. Panel (a) shows the difference between the heat flux leaving the equatorial region and the heat flux into the rest of the atmosphere from the equator from Equations C1 and C3. Similarly Panel (b) shows the difference between the heat flux entering the polar regions and the heat flux from the rest of the atmosphere from Equations C4 and C5. The equatorial region is considered as spanning latitudes of 10°S to 10°N, while the polar regions are 70°S/N to the pole.

$$-\frac{\Delta A_E}{f_E} = \Delta N_E - \Delta U_E - \Delta U_{EA}, \tag{C1}$$

where ΔA_E is the heat transport anomaly between the equatorial region and the rest of the planet. f_E is the equatorial fraction of the global surface (spanning latitudes of 10°S to 10°N, $f_E = 17.4\%$). ΔN_E is the net incoming radiation at the top-of-atmosphere, while ΔU_E is the net upward flux at the surface including both turbulent and radiative fluxes. ΔU_{EA} is the rate of heat storage by the atmosphere over the equatorial region, which is approximated by the globally averaged heat uptake by the atmosphere, ΔU_{GA}:

$$\Delta U_{GA} = \Delta N_G - \Delta U_G, \tag{C2}$$

where the subscript G refers to the global averaged quantities discussed above.

Equivalent expressions can be written for heat flux into the rest of the planet from the equatorial region, as well as the heat flux into the poles and the heat flux from the rest of the atmosphere into the poles:

$$\frac{\Delta A_E}{1 - f_E} = \Delta N_{E'} - \Delta U_{E'} - \Delta U_{E'A}, \tag{C3}$$

$$\frac{\Delta A_P}{f_P} = \Delta N_P - \Delta U_P - \Delta U_{PA}, \tag{C4}$$

$$\frac{\Delta A_P}{1 - f_P} = \Delta N_{P'} - \Delta U_{P'} - \Delta U_{P'A}, \tag{C5}$$

where subscript P represents the polar regions, while E' and P' are the rest of the world excluding the equatorial and polar regions respectively.

This method can be validated by calculating the difference of the heat flux between the equatorial/polar regions and the rest of the atmosphere. These are shown in Figure C1, with the differences more than 1,000 times smaller than 1 W/m^2, showing the self consistency of the method and that it is suitable for applying to understanding heat transport between regions of the atmosphere other than just those over land and sea.

Appendix D: Methane Radiative Forcing: Albedo Dependence

To compare the effect of surface albedo on methane radiative forcing, Figure D1 shows a sensitivity test for two surface albedos of 0.07 (case used in this study) and 0.533, which represents a high value for albedo produced by sand in the near infrared. Figure D1 shows methane radiative forcing after running the model for one additional timestep from the configurations discussed in the main body of text, hence the slight differences between Figure 2 and Figures D1a–D1c. As these are calculated with no evolution of the climate state,

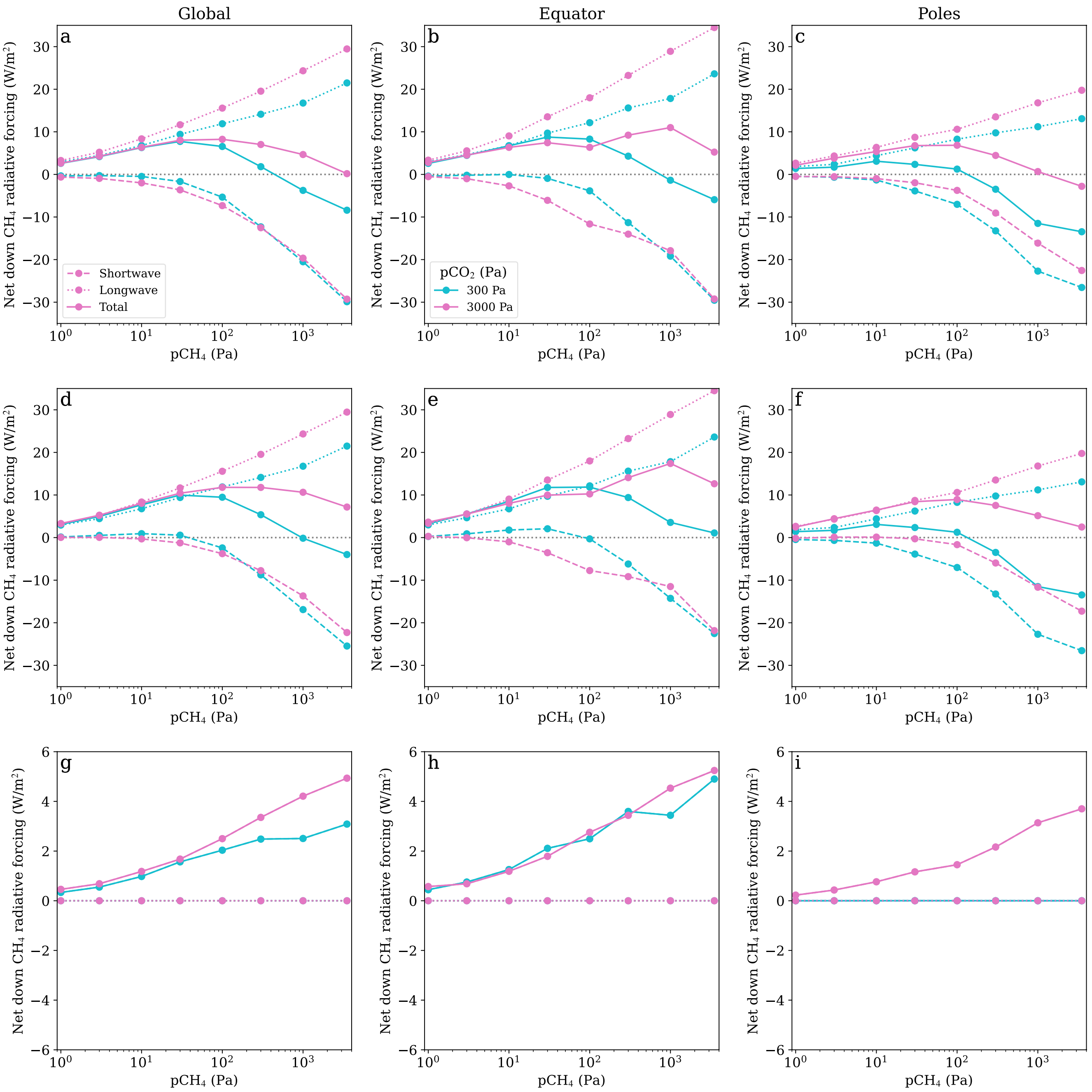

Figure D1. Panel (a) shows the global average net down radiative forcing at the tropopause for methane for shortwave (dashed), longwave (dotted) and their sum (solid), for an ocean surface with an albedo of 0.07. Panels (b and c) show the same as (a) averaged over 10°S to 10°N as the equator in (b), and poleward of 70°N/S for the polar regions in (c). These are calculated for just one model time step. Panels (d–F) shows the same as (a–c) respectively, but for an ocean surface albedo of 0.533. Panels (g–i) show the difference between (a–c) and (d–f), with a positive value indicating an increase in radiative forcing with the higher albedo of 0.533.

there is no change in the longwave radiative forcing between the two cases Figure D1g–i, and the change in shortwave methane radiative forcing is zero at the pole due to this region being ice and ice albedo remains unchanged.

Increasing ocean albedo causes the shortwave methane radiative forcing to decrease, however, general trends in radiative forcings discussed in Section 3 remain the same. At high pCH_4 global temperatures may increase, leading to a less pronounced decline in temperatures compared to those found in Figure 5.

Data Availability Statement

The research data supporting this publication are openly available from the University of Exeter's institutional repository at: https://doi.org/10.24378/exe.4347 with CC BY 4.0 (Eager-Nash et al., 2022).

Acknowledgments

The authors would like to thank the three reviewers for their very helpful reviews that improved the manuscript. The authors would also like to thank Colin Goldblatt for providing helpful comments on the manuscript. JE-N would like to thank the Hill Family Scholarship. The Hill Family Scholarship has been generously supported by University of Exeter Alumnus, and president of the University's US Foundation Graham Hill (Economic & Political Development, 1992) and other donors to the US Foundation. Material produced using Met Office Software. AN, NM and TL gratefully acknowledge funding from a Leverhulme Trust Research Project Grant (RPG-2020-82). SD and TL would like to thank the John Templeton Foundation Grant (62220). JM and IB acknowledge the support of a Met Office Academic Partnership secondment. The authors acknowledge use of the Monsoon2 system, a collaborative facility supplied under the Joint Weather and Climate Research Programme, a strategic partnership between the Met Office and the Natural Environment Research Council. This research made use of the ISCA High Performance Computing Service at the University of Exeter. This work was partly supported by a Science and Technology Facilities Council Consolidated Grant (ST/R000395/1). This work was also supported by a UKRI Future Leaders Fellowship (Grant MR/T040866/1). For the purpose of open access, the author(s) has applied a Creative Commons Attribution (CC BY) licence to any Author Accepted Manuscript version arising. The authors would also like to note the energy intensive nature of super-computing. The authors estimate the final production runs needed for this paper resulted in roughly 4 tCO2e emitted into the atmosphere. For the purpose of open access, the author has applied a ‘Creative Commons Attribution (CC BY) license to any Author Accepted Manuscript version arising'.

References

Andrews, M. B., Ridley, J. K., Wood, R. A., Andrews, T., Blockley, E. W., Booth, B., et al. (2020). Historical simulations with HADGEM3-GC3.1 for CMIP6. *Journal of Advances in Modeling Earth Systems*, *12*(6), e2019MS001995. https://doi.org/10.1029/2019MS001995

Arney, G., Domagal-Goldman, S. D., Meadows, V. S., Wolf, E. T., Schwieterman, E., Charnay, B., et al. (2016). The pale orange dot: The spectrum and habitability of hazy Archean Earth. *Astrobiology*, *16*(11), 873–899. https://doi.org/10.1089/ast.2015.1422

Bartlett, B. C., & Stevenson, D. J. (2016). Analysis of a Precambrian resonance-stabilized day length. *Geophysical Research Letters*, *43*(11), 5716–5724. https://doi.org/10.1002/2016GL068912

Boutle, I. A., Joshi, M., Lambert, F. H., Lyster, D., Manners, J., Mayne, N., et al. (2020). Airborne dust increases the habitability of terrestrial exoplanets. *Nature Communications*, *11*(1), 2731. https://doi.org/10.1038/s41467-020-16543-8

Boutle, I. A., Mayne, N. J., Drummond, B., Manners, J., Goyal, J., Hugo Lambert, F., et al. (2017). Exploring the climate of Proxima B with the Met Office Unified Model. *Astronomy & Astrophysics*, *601*(A120), A120. https://doi.org/10.1051/0004-6361/201630020

Brown, A. R., Beare, R. J., Edwards, J. M., Lock, A. P., Keogh, S. J., Milton, S. F., & Walters, D. N. (2008). Upgrades to the boundary-layer scheme in the met office numerical weather prediction model. *Boundary-Layer Meteorology*, *128*(1), 117–132. https://doi.org/10.1007/s10546-008-9275-0

Brown, L., Sung, K., Benner, D., Devi, V., Boudon, V., Gabard, T., et al. (2013). Methane line parameters in the HITRAN2012 database. *Journal of Quantitative Spectroscopy and Radiative Transfer*, *130*, 201–219. https://doi.org/10.1016/j.jqsrt.2013.06.020

Byrne, B., & Goldblatt, C. (2014). Radiative forcings for 28 potential Archean greenhouse gases. *Climate of the Past*, *10*(5), 1779–1801. https://doi.org/10.5194/cp-10-1779-2014

Byrne, B., & Goldblatt, C. (2015). Diminished greenhouse warming from Archean methane due to solar absorption lines. *Climate of the Past*, *11*(3), 559–570. https://doi.org/10.5194/cp-11-559-2015

Byrom, R. E., & Shine, K. P. (2022). Methane's solar radiative forcing. *Geophysical Research Letters*, *49*(15), e2022GL098270. https://doi.org/10.1029/2022GL098270

Catling, D. C., & Zahnle, K. J. (2020). The Archean atmosphere. *Science Advances*, *6*(9). https://doi.org/10.1126/sciadv.aax1420

Catling, D. C., Zahnle, K. J., & McKay, C. P. (2001). Biogenic methane, hydrogen escape, and the irreversible oxidation of early Earth. *Science*, *293*(5531), 839–843. https://doi.org/10.1126/science.1061976

Cawood, P., Hawkesworth, C., & Dhuime, B. (2013). The continental record and the generation of continental crust. *GSA Bulletin*, *125*(1–2), 14–32. https://doi.org/10.1130/B30722.1

Charnay, B., Forget, F., Wordsworth, R., Leconte, J., Millour, E., Codron, F., & Spiga, A. (2013). Exploring the faint young sun problem and the possible climates of the Archean Earth with a 3-D GCM. *Journal of Geophysical Research: Atmospheres*, *118*(18), 10414–10431. https://doi.org/10.1002/jgrd.50808

Charnay, B., Le Hir, G., Fluteau, F., Forget, F., & Catling, D. C. (2017). A warm or a cold early Earth? New insights from a 3-D climate-carbon model. *Earth and Planetary Science Letters*, *474*, 97–109. https://doi.org/10.1016/j.epsl.2017.06.029

Charnay, B., Wolf, E. T., Marty, B., & Forget, F. (2020). Is the faint young sun problem for Earth solved? *Space Science Reviews*, *216*(5), 90. https://doi.org/10.1007/s11214-020-00711-9

Claire, M. W., Catling, D. C., & Zanhle, K. J. (2006). Biogeochemical modelling of the rise in atmospheric oxygen. *Geobiology*, *4*(4), 239–269. https://doi.org/10.1111/j.1472-4669.2006.00084.x

Claire, M. W., Sheets, J., Cohen, M., Ribas, I., Meadows, V. S., & Catling, D. C. (2012). The evolution of solar flux from 0.1 nm TO 160 μm: Quantitative estimates for planetary studies. *The Astrophysical Journal*, *757*(1), 95. https://doi.org/10.1088/0004-637x/757/1/95

Collins, W. D., Feldman, D. R., Kuo, C., & Nguyen, N. H. (2018). Large regional shortwave forcing by anthropogenic methane informed by Jovian observations. *Science Advances*, *4*(9), eaas9593. https://doi.org/10.1126/sciadv.aas9593

Daines, S. J., & Lenton, T. M. (2016). The effect of widespread early aerobic marine ecosystems on methane cycling and the great oxidation. *Earth and Planetary Science Letters*, *434*, 42–51. https://doi.org/10.1016/j.epsl.2015.11.021

Domagal-Goldman, S. D., Kasting, J. F., Johnston, D. T., & Farquhar, J. (2008). Organic haze, glaciations and multiple sulfur isotopes in the mid-Archean era. *Earth and Planetary Science Letters*, *269*(1), 29–40. https://doi.org/10.1016/j.epsl.2008.01.040

Dong, J., Fischer, R. A., Stixrude, L. P., & Lithgow-Bertelloni, C. R. (2021). Constraining the volume of Earth's early oceans with a temperature-dependent mantle water storage capacity model. *AGU Advances*, *2*(1), e2020AV000323. https://doi.org/10.1029/2020AV000323

Donohoe, A., & Battisti, D. S. (2011). Atmospheric and surface contributions to planetary albedo. *Journal of Climate*, *24*(16), 4402–4418. https://doi.org/10.1175/2011JCLI3946.1

Driese, S., Jirsa, M., Ren, M., Brantley, S., Sheldon, N., Parker, D., & Schmitz, M. (2011). Neoarchean paleoweathering of tonalite and metabasalt: Implications for reconstructions of 2.69Ga early terrestrial ecosystems and paleoatmospheric chemistry. *Precambrian Research*, *189*(1–2), 1–17. https://doi.org/10.1016/j.precamres.2011.04.003

Eager-Nash, J. K., Reichelt, D. J., Mayne, N. J., Hugo Lambert, F., Sergeev, D. E., Ridgway, R. J., et al. (2020). Implications of different stellar spectra for the climate of tidally locked Earth-like exoplanets. *A&A*, *639*(A99). https://doi.org/10.1051/0004-6361/202038089

Eager-Nash, J. K., Mayne, N. J., Nicholson, A. E., Prins, J. E., Young, O. C. F., Daines, S. J., et al. (2022). 3D climate simulations of the Archean find that methane has a strong cooling effect at high concentrations [dataset]. Open Research Exeter (ORE). https://doi.org/10.24378/exe.4347

Eigenbrode, J. L., & Freeman, K. H. (2006). Late Archean rise of aerobic microbial ecosystems. *Proceedings of the National Academy of Sciences of the United States of America*, *103*(43), 15759–15764. https://doi.org/10.1073/pnas.0607540103

Etminan, M., Myhre, G., Highwood, E. J., & Shine, K. P. (2016). Radiative forcing of carbon dioxide, methane, and nitrous oxide: A significant revision of the methane radiative forcing. *Geophysical Research Letters*, *43*(24), 12614–12623. https://doi.org/10.1002/2016GL071930

Feulner, G. (2012). The faint young sun problem. *Reviews of Geophysics*, *50*(2). https://doi.org/10.1029/2011RG000375

Flament, N., Coltice, N., & Rey, P. F. (2008). A case for late-Archaean continental emergence from thermal evolution models and hypsometry. *Earth and Planetary Science Letters*, *275*(3), 326–336. https://doi.org/10.1016/j.epsl.2008.08.029

Frierson, D. M. W., Held, I. M., & Zurita-Gotor, P. (2006). A gray-radiation aquaplanet moist GCM. Part I: Static stability and eddy scale. *Journal of the Atmospheric Sciences*, *63*(10), 2548–2566. https://doi.org/10.1175/jas3753.1

Goldblatt, C., Lenton, T. M., & Watson, A. J. (2006). Bistability of atmospheric oxygen and the great oxidation. *Nature*, *443*(7112), 683–686. https://doi.org/10.1038/nature05169

Goldblatt, C., McDonald, V. L., & McCusker, K. E. (2021). Earth's long-term climate stabilized by clouds. *Nature Geoscience*, *14*(3), 143–150. https://doi.org/10.1038/s41561-021-00691-7

Gough, D. O. (1981). Solar interior structure and luminosity variations. *Solar Physics*, *74*(1), 21–34. https://doi.org/10.1007/BF00151270

Gregory, B. S., Claire, M. W., & Rugheimer, S. (2021). Photochemical modelling of atmospheric oxygen levels confirms two stable states. *Earth and Planetary Science Letters*, *561*, 116818. https://doi.org/10.1016/j.epsl.2021.116818

Gregory, D., & Rowntree, P. R. (1990). A mass flux convection scheme with representation of cloud ensemble characteristics and stability-dependent closure. *Monthly Weather Review*, *118*(7), 1483–1506. https://doi.org/10.1175/1520-0493(1990)118<1483:amfcsw>2.0.co;2

Haqq-Misra, J. D., Domagal-Goldman, S. D., Kasting, P. J., & Kasting, J. F. (2008). A revised, hazy methane greenhouse for the Archean Earth. *Astrobiology*, *8*(6), 1127–1137. https://doi.org/10.1089/ast.2007.0197

Hargreaves, R. J., Gordon, I. E., Rey, M., Nikitin, A. V., Tyuterev, V. G., Kochanov, R. V., & Rothman, L. S. (2020). An accurate, extensive, and practical line list of methane for the HITEMP database. *The Astrophysical Journal*, *247*(2), 55. https://doi.org/10.3847/1538-4365/ab7a1a

Hawkesworth, C., Cawood, P. A., & Dhuime, B. (2019). Rates of generation and growth of the continental crust. *Geoscience Frontiers*, *10*(1), 165–173. https://doi.org/10.1016/j.gsf.2018.02.004

Huang, G., Eager, J., Mayne, N., Cui, D., Manners, J., Hebrard, E., et al. (2021). CO_2 and O_2 oxidized 2.7 Ga micrometeorites in two stages suggesting a > 32% CO_2 atmosphere. *Precambrian Research*, *366*, 106423. https://doi.org/10.1016/j.precamres.2021.106423

Hunter, J. D. (2007). Matplotlib: A 2D graphics environment. *Computing in Science & Engineering*, *9*(3), 90–95. https://doi.org/10.1109/MCSE.2007.55

Izon, G., Zerkle, A. L., Zhelezinskaia, I., Farquhar, J., Newton, R. J., Poulton, S. W., et al. (2015). Multiple oscillations in Neoarchaean atmospheric chemistry. *Earth and Planetary Science Letters*, *431*, 264–273. https://doi.org/10.1016/j.epsl.2015.09.018

Jin, Z., Charlock, T. P., Smith, W. L., Jr., & Rutledge, K. (2004). A parameterization of ocean surface albedo. *Geophysical Research Letters*, *31*(22), L22301. https://doi.org/10.1029/2004GL021180

Joshi, M. M., & Haberle, R. M. (2012). Suppression of the water ice and snow albedo feedback on planets orbiting red dwarf stars and the subsequent widening of the habitable zone. *Astrobiology*, *12*(1), 3–8. https://doi.org/10.1089/ast.2011.0668

Kanzaki, Y., & Murakami, T. (2015). Estimates of atmospheric CO2 in the Neoarchean-Paleopr$_o$terozoic from paleosols. *Geochimica et Cosmochimica Acta*, *159*, 190–219. https://doi.org/10.1016/j.gca.2015.03.011

Karman, T., Gordon, I. E., van der Avoird, A., Baranov, Y. I., Boulet, C., Drouin, B. J., et al. (2019). Update of the HITRAN collision-induced absorption section. *Icarus*, *328*, 160–175. https://doi.org/10.1016/j.icarus.2019.02.034

Kaspi, Y., & Showman, A. P. (2015). Atmospheric dynamics of terrestrial exoplanets over a wide range of orbital and atmospheric parameters. *The Astrophysical Journal*, *804*(1), 60. https://doi.org/10.1088/0004-637x/804/1/60

Kasting, J. F. (2005). Methane and climate during the Precambrian era. *Precambrian Research*, *137*(3), 119–129. https://doi.org/10.1016/j.precamres.2005.03.002

Kasting, J. F., & Catling, D. (2003). Evolution of a habitable planet. *Annual Review of Astronomy and Astrophysics*, *41*(1), 429–463. https://doi.org/10.1146/annurev.astro.41.071601.170049

Kavanagh, L., & Goldblatt, C. (2015). Using raindrops to constrain past atmospheric density. *Earth and Planetary Science Letters*, *413*, 51–58. https://doi.org/10.1016/j.epsl.2014.12.032

Kharecha, P., Kasting, J., & Siefert, J. (2005). A coupled atmosphere–ecosystem model of the early Archean Earth. *Geobiology*, *3*(2), 53–76. https://doi.org/10.1111/j.1472-4669.2005.00049.x

Kopp, G., Krivova, N., Wu, C. J., & Lean, J. (2016). The impact of the revised sunspot record on solar irradiance reconstructions. *Solar Physics*, *291*(9), 2951–2965. https://doi.org/10.1007/s11207-016-0853-x

Kunze, M., Godolt, M., Langematz, U., Grenfell, J., Hamann-Reinus, A., & Rauer, H. (2014). Investigating the early Earth faint young sun problem with a general circulation model. *Planetary and Space Science*, *98*, 77–92. https://doi.org/10.1016/j.pss.2013.09.011

Lambert, F. H., Webb, M. J., & Joshi, M. M. (2011). The relationship between land–ocean surface temperature contrast and radiative forcing. *Journal of Climate*, *24*(13), 3239–3256. https://doi.org/10.1175/2011JCLI3893.1

Le Hir, G., Teitler, Y., Fluteau, F., Donnadieu, Y., & Philippot, P. (2014). The faint young sun problem revisited with a 3-D climate–carbon model – Part 1. *Climate of the Past*, *10*(2), 697–713. https://doi.org/10.5194/cp-10-697-2014

Lewis, N. T., Lambert, F. H., Boutle, I. A., Mayne, N. J., Manners, J., & Acreman, D. M. (2018). The influence of a substellar continent on the climate of a tidally locked exoplanet. *The Astrophysical Journal*, *854*(2), 171. https://doi.org/10.3847/1538-4357/aaad0a

Liu, J., Zhang, Z., Inoue, J., & Horton, R. M. (2007). Evaluation of snow/ice albedo parameterizations and their impacts on sea ice simulations. *International Journal of Climatology*, *27*(1), 81–91. https://doi.org/10.1002/joc.1373

Lock, A. P., Brown, A. R., Bush, M. R., Martin, G. M., & Smith, R. N. B. (2000). A new boundary layer mixing scheme. Part I: Scheme description and single-column model tests. *Monthly Weather Review*, *128*(9), 3187–3199. https://doi.org/10.1175/1520-0493(2000)128<3187:anblms>2.0.co;2

Maher, P., & Earnshaw, P. (2022). The flexible modelling framework for the met office unified model (flex-um, using um 12.0 release). *Geoscientific Model Development*, *15*(3), 1177–1194. https://doi.org/10.5194/gmd-15-1177-2022

Mayne, N. J., Baraffe, I., Acreman, D. M., Smith, C., Wood, N., Amundsen, D. S., et al. (2014). Using the UM dynamical cores to reproduce idealised 3-D flows. *Geoscientific Model Development*, *7*(6), 3059–3087. https://doi.org/10.5194/gmd-7-3059-2014

Met Office. (2010–2020). Iris: A Python library for analysing and visualising meteorological and oceanographic data sets (v2.4 ed.). Retrieved from http://scitools.org.uk/

Nicholson, A. E., Daines, S. J., Mayne, N. J., Eager-Nash, J. K., Lenton, T. M., & Kohary, K. (2022). Predicting biosignatures for nutrient-limited biospheres. *Monthly Notices of the Royal Astronomical Society*, *517*(1), 222–239. https://doi.org/10.1093/mnras/stac2086

Poulsen, C. J., & Jacob, R. L. (2004). Factors that inhibit snowball Earth simulation. *Paleoceanography*, *19*(4), PA4021. https://doi.org/10.1029/2004PA001056

Rimmer, P. B., Shorttle, O., & Rugheimer, S. (2019). Oxidised micrometeorites as evidence for low atmospheric pressure on the early Earth. *Geochemical Perspectives Letters*, *9*, 38–42. https://doi.org/10.7185/geochemlet.1903

Rothman, L., Gordon, I., Babikov, Y., Barbe, A., Chris Benner, D., Bernath, P., et al. (2013). The HITRAN2012 molecular spectroscopic database. *Journal of Quantitative Spectroscopy and Radiative Transfer*, *130*, 4–50. https://doi.org/10.1016/j.jqsrt.2013.07.002

Sagan, C., & Mullen, G. (1972). Earth and Mars: Evolution of atmospheres and surface temperatures. *Science*, *177*(4043), 52–56. https://doi.org/10.1126/science.177.4043.52

Sellar, A. A., Jones, C. G., Mulcahy, J. P., Tang, Y., Yool, A., Wiltshire, A., et al. (2019). Ukesm1: Description and evaluation of the u.k. Earth system model. *Journal of Advances in Modeling Earth Systems*, *11*(12), 4513–4558. https://doi.org/10.1029/2019MS001739

Sergeev, D. E., Fauchez, T. J., Turbet, M., Boutle, I. A., Tsigaridis, K., Way, M. J., et al. (2021). The TRAPPIST-1 habitable atmosphere intercomparison (THAI). Part II: Moist cases – the two waterworlds. arXiv. https://doi.org/10.48550/ARXIV.2109.11459

Sergeev, D. E., Lambert, F. H., Mayne, N. J., Boutle, I. A., Manners, J., & Kohary, K. (2020). Atmospheric convection plays a key role in the climate of tidally locked terrestrial exoplanets: Insights from high-resolution simulations. *The Astrophysical Journal*, *894*(2), 84. https://doi.org/10.3847/1538-4357/ab8882

Sergeev, D. E., & Zamyatina, M. (2022). Aeolus. *Zenodo*. https://doi.org/10.5281/zenodo.6478085

Sheldon, N. D. (2006). Precambrian paleosols and atmospheric CO_2 levels. *Precambrian Research*, *147*(1), 148–155. https://doi.org/10.1016/j.precamres.2006.02.004

Snyder, W. C., Wan, Z., Zhang, Y., & Feng, Y.-Z. (1998). Classification-based emissivity for land surface temperature measurement from space. *International Journal of Remote Sensing*, *19*(14), 2753–2774. https://doi.org/10.1080/014311698214497

Som, S. M., Buick, R., Hagadorn, J. W., Blake, T. S., Perreault, J. M., Harnmeijer, J. P., & Catling, D. C. (2016). Earth's air pressure 2.7 billion years ago constrained to less than half of modern levels. *Nature Geoscience*, *9*(6), 448–451. https://doi.org/10.1038/ngeo2713

Som, S. M., Catling, D. C., Harnmeijer, J. P., Polivka, P. M., & Buick, R. (2012). Air density 2.7 billion years ago limited to less than twice modern levels by fossil raindrop imprints. *Nature*, *484*(7394), 359–362. https://doi.org/10.1038/nature10890

Teitler, Y., Le Hir, G., Fluteau, F., Philippot, P., & Donnadieu, Y. (2014). Investigating the Paleoproterozoic glaciations with 3-d climate modeling. *Earth and Planetary Science Letters*, *395*, 71–80. https://doi.org/10.1016/j.epsl.2014.03.044

Tomkins, A. G., Bowlt, L., Genge, M., Wilson, S. A., Brand, H. E. A., & Wykes, J. L. (2016). Ancient micrometeorites suggestive of an oxygen-rich archaean upper atmosphere. *Nature*, *533*(7602), 235–238. https://doi.org/10.1038/nature17678

Trainer, M. G., Pavlov, A. A., DeWitt, H. L., Jimenez, J. L., McKay, C. P., Toon, O. B., & Tolbert, M. A. (2006). Organic haze on titan and the early Earth. *Proceedings of the National Academy of Sciences*, *103*(48), 18035–18042. https://doi.org/10.1073/pnas.0608561103

Turbet, M., Boulet, C., & Karman, T. (2020). Measurements and semi-empirical calculations of CO_2+CH_4 and CO_2+H_2 collision-induced absorption across a wide range of wavelengths and temperatures. Application for the prediction of early Mars surface temperature. *Icarus*, *346*, 113762. https://doi.org/10.1016/j.icarus.2020.113762

Walker, J. C. G. (1987). Was the Archaean biosphere upside down? *Nature*, *329*(6141), 710–712. https://doi.org/10.1038/329710a0

Walters, D., Baran, A. J., Boutle, I., Brooks, M., Earnshaw, P., Edwards, J., et al. (2019). The met office unified model global atmosphere 7.0/7.1 and Jules global land 7.0 configurations. *Geoscientific Model Development*, *12*(5), 1909–1963. https://doi.org/10.5194/gmd-12-1909-2019

Williams, G. E. (2000). Geological constraints on the Precambrian history of Earth's rotation and the Moon's orbit. *Reviews of Geophysics*, *38*(1), 37–59. https://doi.org/10.1029/1999RG900016

Wilson, D. R., & Ballard, S. P. (1999). A microphysically based precipitation scheme for the UK meteorological office unified model. *Quarterly Journal of the Royal Meteorological Society*, *125*(557), 1607–1636. https://doi.org/10.1002/qj.49712555707

Wilson, D. R., Bushell, A. C., Kerr-Munslow, A. M., Price, J. D., & Morcrette, C. J. (2008). PC2: A prognostic cloud fraction and condensation scheme. I: Scheme description. *Quarterly Journal of the Royal Meteorological Society*, *134*(637), 2093–2107. https://doi.org/10.1002/qj.333

Wolf, E., & Toon, O. (2013). Hospitable Archean climates simulated by a general circulation model. *Astrobiology*, *13*(7), 656–673. https://doi.org/10.1089/ast.2012.0936

Wolf, E., & Toon, O. (2014). Controls on the Archean climate system investigated with a global climate model. *Astrobiology*, *14*(3), 241–253. https://doi.org/10.1089/ast.2013.1112

Wood, N., Staniforth, A., White, A., Allen, T., Diamantakis, M., Gross, M., et al. (2014). An inherently mass-conserving semi-implicit semi-Lagrangian discretization of the deep-atmosphere global non-hydrostatic equations. *Quarterly Journal of the Royal Meteorological Society*, *140*(682), 1505–1520. https://doi.org/10.1002/qj.2235

World Meteorological Organisation. (1957). Meteorology: A three-dimensional science, second session of the commission for aerology. *World Meteorological Organization Bulletin*, *6*(4), 134–138.

Yates, J. S., Palmer, P. I., Manners, J., Boutle, I., Kohary, K., Mayne, N., & Abraham, L. (2020). Ozone chemistry on tidally locked M dwarf planets. *Monthly Notices of the Royal Astronomical Society*, *492*(2), 1691–1705. https://doi.org/10.1093/mnras/stz3520

Yurchenko, S. N., & Tennyson, J. (2014). ExoMol line lists – IV. The rotation–vibration spectrum of methane up to 1500 K. *Monthly Notices of the Royal Astronomical Society*, *440*(2), 1649–1661. https://doi.org/10.1093/mnras/stu326